University of Massachusetts Amherst

ScholarWorks@UMass Amherst

March 2024

Multi-method Approach to Assess the Impact of Off-fault Deformation During Fault Evolution

Christ Faviana Ramos Sanchez

Follow this and additional works at: https://scholarworks.umass.edu/masters_theses_2

Multi-method Approach to Assess the Impact of Off-fault Deformation During Fault
Evolution

A Thesis Presented

by

CHRIST FAVIANA RAMOS SÁNCHEZ

Submitted to the Graduate School of the
University of Massachusetts Amherst in partial fulfillment
of the requirements for the degree of

MASTER OF SCIENCE

February 2024

Department of Earth, Geographic, and Climate Sciences

Multi-method Approach to Assess the Impact of Off-fault Deformation During Fault Evolution

A Thesis Presented

By

CHRIST FAVIANA RAMOS SÁNCHEZ

Approved as to style and content by:

_____

Michele Cooke, Chair

_____

Haiying Gao, Member

_____

Jack Loveless, Member

_____

Piper Gaubatz, Department Head

Department of Earth, Geographic, and Climate Sciences

ABSTRACT

MULTI-METHOD APPROACH TO ASSESS THE IMPACT OF OFF-FAULT

DEFORMATION DURING FAULT EVOLUTION

FEBRUARY 2024

CHRIST FAVIANA RAMOS SÁNCHEZ

M.S., UNIVERSITY OF MASSACHUSETTS AMHERST

Directed by: Dr. Michele Cooke

Scaled physical experiments using analog materials that simulate deformation processes in the Earth's crust provide direct observations of deformation during strike-slip fault evolution. Carefully scaled experiments allow us to directly observe millions of years of deformation within hours and document the behavior of experimental faults. My thesis is composed of three distinct chapters that use scaled physical experiments to help us better understand partitioning of deformation on and off of strike-slip faults within the Earth's crust. For my first project, I built a workflow that allows the measurement of off-fault deformation manifested as vertical motions along faults. When combined with horizontal displacements, these measurements allow us to quantify off-fault deformation in three dimensions during strike-slip fault experiments conducted in the geomechanics laboratory. My second project, inspired by the 2019 Ridgecrest earthquake, investigates the impact of pre-existing weaknesses during strike-slip fault evolution using scaled physical experiments with wet kaolin that simulate upper crustal deformation processes. Pre-existing weaknesses oriented 90-120˚ (counter-clockwise) from the primary fault experience left-lateral slip that matches coseismic observations from the northern portion of the Ridgecrest main shock rupture. My third and final project utilizes results from experimental strike-slip faults on wet kaolin and dry sand (both poured and sedimented) to train convolutional neural networks (CNN) to predict off-fault deformation from maps of active strike-slip faults of different maturity such as those in southern California. The

different analog materials produce different estimates of off-fault deformation along strike-slip faults due to the different portioning of strain on and off of faults within the materials. Whether due to material properties or active fault geometry, regions of greater off-fault deformation in the crust have greater shallow slip deficit so that surface estimates of deformation may underestimate sub-surface seismic hazard.

TABLE OF CONTENTS

LIST OF TABLES

LIST OF FIGURES

CHAPTER 1

STRUCTURE FROM MOTION

1.1 Introduction

As strike-slip faults evolve, strain is both localized along and distributed around active faults. Distributed strain away from the fault, known as off-fault deformation, is manifested through deformation of the crust in three dimensions, such as distortional and dilatational strain of material along faults (e.g., Toeneboehn et al., 2018). Geologic field observations only provide us with the final cumulative information about off-fault deformation around strike-slip faults but do not directly inform its evolution.

To investigate fault evolution, experimental strike-slip faults that are carefully scaled to represent faulting processes within the upper crust provide us with direct information about strain partitioning of strike-slip faults as they evolve. While fault evolution in the crust occurs at length scales and time that are impossible to directly observe, we can record such deformation within table-top experiments. Wet kaolin strike-slip fault experiments are capable of simulating crustal fault evolution because the properties and length scaling of the clay have been previously well-studied and serve as a good analog for the crust (e.g., Cooke et al., 2013; Cooke & Van Der Elst, 2012; Hatem et al., 2015, 2017; Henza et al., 2010). Previous studies use Digital Image Correlation methods to accurately measure the horizontal slip components and strain partitioning of faults throughout experiments (e.g., Elston et al., 2022; Hatem et al., 2015, 2017; Toeneboehn et al., 2018). What is missing from those horizontal displacement fields is the vertical change in clay surface elevation that reveals both localized dip-slip on faults

and distributed off-fault deformation. To calculate this vertical off-fault deformation associated with strike-slip faults as they evolve, Toeneboehn et al. (2018) used a stereo vision method. However, this method is no longer in-use by the UMass geomechanics laboratory as it requires lengthy and unreliable calibration of photos.

Since the change in uplift/subsidence of the surface of the wet kaolin adjacent to strike-slip faults may only vary by a few millimeters in elevation, we need fine vertical resolution to capture the incremental elevation of the topography throughout all stages of the experiment. Therefore, our goal is to find the most efficient tool and workflow that will allow reliable and detailed measurement of uplift/subsidence. To quantify off-fault deformation evolution in three dimensions we need time series of both horizontal and vertical displacement fields throughout the experiment. Here, I describe an efficient Structure from Motion workflow (Bemis et al., 2014), using Agisoft Metashape software, that provides sufficient resolution of uplift throughout the experiments to inform off-fault deformation around strike-slip faults.

1.2 Methods

Our workflow is composed of seven steps that take place after the wet kaolin has been prepared and placed in the claybox (Figure 1.1).

```
┌─────────────────────┐
│ Position and calibrate all │
│ cameras             │
└─────────────────────┘
          ⇩
┌─────────────────────┐
│ Place control points on │
│ the clay's surface  │
└─────────────────────┘
          ⇩
┌─────────────────────┐
│ Run experiment      │
└─────────────────────┘
          ⇩
┌─────────────────────┐
│ Create folders with │
│ corresponding pictures │
│ and control point   │
│ location for each stage │
│ of the experiment   │
└─────────────────────┘
          ⇩
┌─────────────────────┐
│ Generate point cloud in │
│ Metashape           │
└─────────────────────┘
          ⇩
┌─────────────────────┐
│ Import point cloud to │
│ Matlab for fine tuning │
└─────────────────────┘
          ⇩
┌─────────────────────┐
│ Create uplift movie │
└─────────────────────┘
```
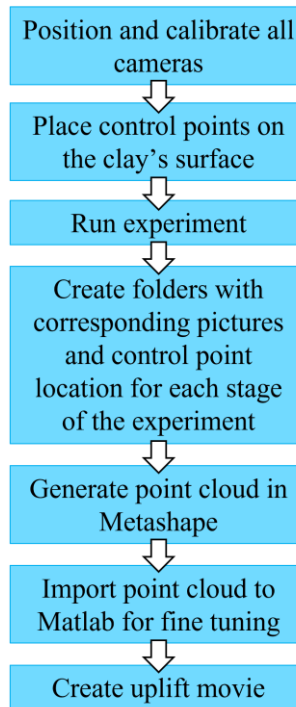
Figure 1.1: Workflow of the seven-step experimental method.

1.2.1 Measuring Incremental Uplift/Subsidence

Structure from Motion uses many photographs taken from a range of positions and directions to produce a composite three-dimensional point cloud using dense stereo matching (e.g., Bemis et al., 2014). Here, we analyze changes in the experiment topography revealed by the point cloud to investigate the distribution of off-fault deformation as faults evolve. Previous studies used stereovision (Toeneboehn et al., 2018) or other open-source Structure from Motion software such as MicMac (Visage et al., 2023) to calculate the horizontal and vertical deformation of the experiment surface. However, they require overly complicated camera calibration, lengthy correlation methods, and higher computer power (Toeneboehn et al., 2018). We use Metashape software by Agisoft because it provides efficient and swift results with a single tool.

Metashape can process over 50,000 photos (either aerial, close-range, or satellite) at once and form 3D spatial data in the form of dense point clouds that can eventually be used to create textured polygonal models, or a georeferenced orthomosaic. Metashape considers the interior and exterior orientation parameters of overlapping image pairs to generate multiple pairwise depth maps for each camera. The pairwise depth maps are then merged into a single depth map, for each camera, that has redundant information within the overlapped regions to filter wrong depth measurements. Afterwards, each combined depth map produced for each camera is merged to create a partial dense point cloud that goes through an additional noise filtering step applied in the overlapping regions to finally make the dense point cloud ("Agisoft Metashape: User Manuals").

For our experiments we use only 5 simultaneous photos taken from different angles to create the 3D surface. To reduce the errors that would arise from using only 5 photos we incorporate the known 3D coordinate location for each control point added on the top of the clay surface and on the edges of the claybox. These ground control points increase the accuracy of the dense point cloud during the dense stereo matching. We can generate robust 3D point clouds that have millions of points of data (with known x, y, and z coordinates) of the complete surface of the clay during any time frame of the experiment simply by using 5 sets of pictures and 12 control points as inputs.

1.2.1.1 Wet Kaolin

Physical experiments on a tabletop are 5 orders of magnitude smaller in spatial scale than faults within the crust. Hence, the analog material (wet kaolin) is also 5 orders

of magnitude weaker than crustal rocks (e.g., Cooke et al., 2013; Hatem et al., 2015, 2017; Henza et al., 2010). During experiments, 1 cm in the claybox apparatus represents 1-2 km of the crust (Hatem et al., 2017; Henza et al., 2010). Prior to each experiment, we adjust the water content of the wet kaolin to achieve the shear strength that maintains this claybox : crust length scaling. Wet kaolin's particle size distribution is 5-10% of sand, 30-35% of silt, and 60% of clay sized particle by mass (Hatem et al., 2017) with a water content of 60-65% and shear strengths around 100-110 Pa (Cooke et al., 2013; Hatem et al., 2017; Henza et al., 2010). Wet kaolin is often used to replicate fault experiments because it produces visible and sharp faults that are easy to trace throughout the experiment (Eisenstadt & Sims, 2005; Henza et al., 2010). Furthermore, wet kaolin has the ability of producing long-lived faults due its low but non-zero shear strength (Cooke et al., 2013; Eisenstadt & Sims, 2005; Withjack et al., 2007) and it can simulate off-fault relaxation of the crust due to its viscoelastic behavior (Cooke & Van Der Elst, 2012).

1.2.1.1.1 Claybox, Template, and Control Points

Within the laboratory we simulate crustal fault evolution with the experimental claybox (or also known as split box), which is a motor-controlled, tabletop apparatus (e.g. Hatem et al., 2017). The claybox has two pieces: one is a static plate that remains fixed to the table and the other plate is attached to stepper motors and moves at a prescribed speed (mm/min) and direction (Figure 1.2). The claybox has a length of 50 cm but it can have width ranging from 25 cm to 30 cm, depending on the experiment configuration and the desired basal condition. Since the claybox remains with the same length but varies in width, I designed and created a Plexiglass template (Figure 1.2) to guide the accurate and

consistent placement of the cylindrical control points for all experiments, even those with

different claybox widths.
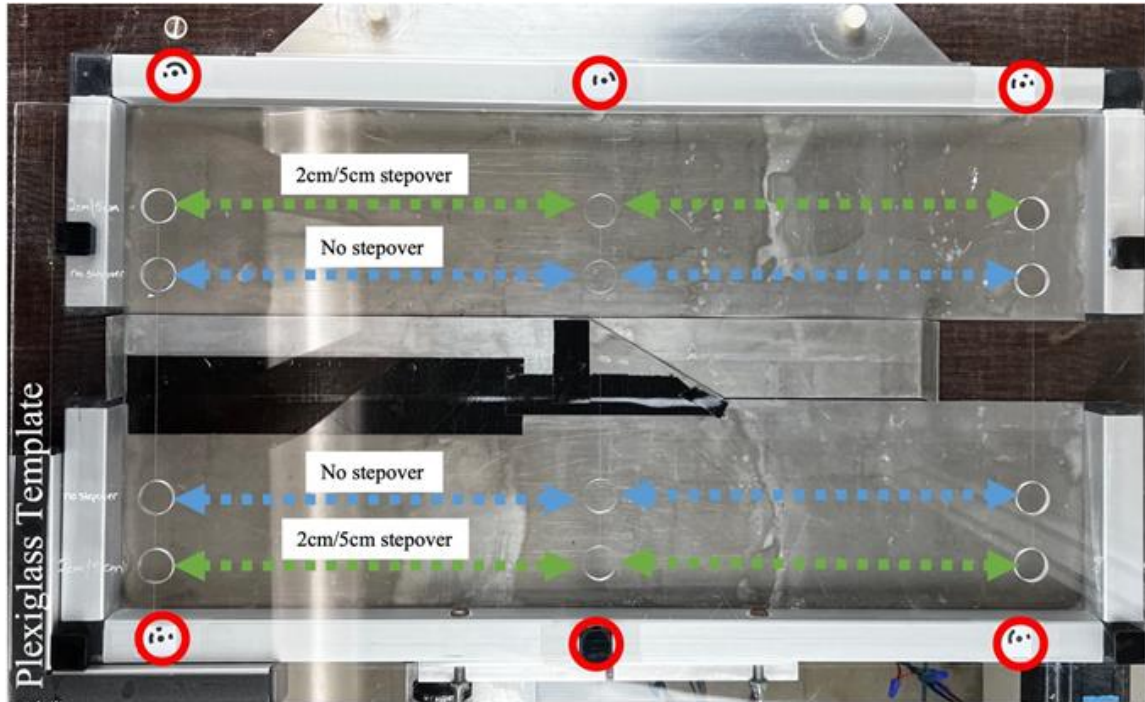
Figure 1.2: Plexiglass template designed to control the placement of six control points on top of the wet kaolin prior to running the experiments. Green arrows denote the holes designed for strike slip fault experiments with 2 cm or 5 cm stepover and blue arrows indicate holes to use when conducting strike-slip fault experiment with no stepover. The red circles denote the six permanent control points located on the edges of the moving plate and static plate of the claybox apparatus.

The Structure from Motion technique optimizes uplift resolution using the known

positions of control points. I designed six lightweight 3D cylinders that function as

control points located on top of the surface of the wet kaolin (Figure 1.3) and added six

more control points (three placed on the static plate and three on the moving plate) on the

outside walls of the claybox (Figure 1.2). All six 3D cylinders have the same diameter

but different heights (Figure 1.3). The height varies from 2 mm to 22 mm (with

increasing height of 4 mm each) to span the range of cumulative elevation typically

generated within strike-slip fault experiments.
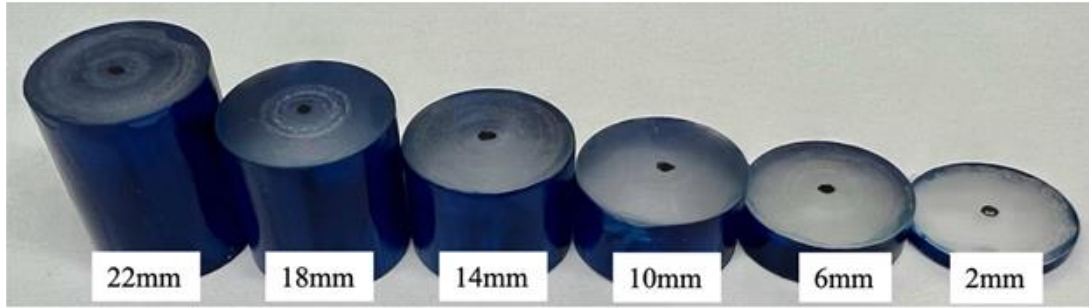
Figure 1.3: Control points designed in different heights for the claybox. Each cylinder sits directly on the clay surface.

The one-dimensional control points located on the outer walls of the claybox

provide greater accuracy than just using the six cylinders as ground control points. We

secured to the claybox outer walls paper-printed control points provided by the software

that can be automatically detected by Metashape. All control points have known x, y, and

z coordinates at the onset of the experiment and their positions are tracked throughout the

experiment. Placing the cylinders on top of the wet kaolin with known coordinates plus

six more one dimensional control points aligned on the edges of the claybox greatly

improves the resolution of the topography of the clay. The three 3D cylinders and three

one dimensional control points on the moving plate (Figure 1.2) will shift in the x-

direction as the stepper motors transport the moving plate. Because of this shift in

position, we wrote a script that uses the horizontal displacement field data to adjust the x

position of each control point during any time frame during the experiment. When

generating a dense point cloud at a particular stage of the experiment, we can calculate the three-dimensional position of each control point at that stage of the experiment.

1.2.1.1.1.1 Cameras Position and Calibration

Because uplift/subsidence of the surface of the wet kaolin around strike-slip faults only ranges from a few millimeters up to 2 cm in elevation, we need fine vertical resolution to capture the incremental elevation of the topography throughout all stages of the experiment. We used five Canon cameras (two Canon Rebel T3i and three Canon Rebel SL3) with standard 18-55mm lenses and polarized light lenses to improve image quality by increasing focal length and avoiding glare of the horizontal edges of the claybox. To provide a variety of look angles of the surface of the clay, we placed four cameras, with zoom and polarized light lenses, on each corner of the claybox and a fifth camera directly above the center of the box. After setting up each camera and before running the experiment, we need to calibrate all cameras with a uniform black and white chessboard grid.

Because each of the five cameras is set up at different angles and distances, we must perform a new calibration any time that the position or zoom length of a camera is adjusted. Once all cameras are accurately positioned and focused as desired, we took at least 3 pictures from each camera of the chessboard pattern that we placed on top of the claybox spanning the desired field view. These photos are used to calibrate the camera positions and look angles into a single consistent world view. Once all pictures of the chessboard pattern are taken for all cameras, we cannot perturb the cameras throughout the duration of the experiment.

The central camera is placed at a height that fully captures the region of interest within the claybox and the photos are used for both structure from motion and generating incremental horizontal displacement fields via Digital Image Correlation. We only used lens corrected (undistorted) series of photos from the top camera for the incremental displacement field. We performed undistortion of all pictures taken from the top camera in batches using Adobe Photoshop, which also allows us to turn all color images in black and white to reduce file size and expedite image analysis. We do not employ this undistortion step to the photos from the remaining four cameras because Agisoft Metashape Professional Edition has an automatic calibration step for the full camera matrix that includes non-linear distortion coefficients.

Because we rely on the images from the central camera to generate the incremental horizontal displacement fields, the central camera takes frequent pictures throughout the experiment, which generates hundreds of pictures. This allows us to detect horizontal strain field maps with <1 mm spacing and calculate strike-slip rates along faults (Elston et al., 2022). On the other hand, because the vertical movement associated with strike-slip faults is much slower than the horizontal movement, the remaining four cameras, set at varying angles and zoom length, capture less frequent pictures than the top camera. Because the remaining cameras take pictures less frequently than the top camera, we wrote a script that creates folders of images corresponding to the same stage of the experiment. This is a significant step in the workflow because we need all corresponding five pictures (one image taken per camera) of the same stage for the purpose of aligning them and creating the final dense point cloud of the surface of the clay to resolve the vertical displacement of that one timeframe.

1.2.1.1.1.1.1 Analyzing Uplift/Subsidence

Once we have the final dense point cloud representing the topography of the clay surface (Figure 1.4), we import the point cloud into Matlab™ for processing. I designed a script that down samples the unrefined dense point cloud, crops to the area of interest, and performs subtle noise filtering (3x3 median filter) to generate the final surface map (Figure 1.5a) that we later use for analysis of the uplift/subsidence rate of the clay surface. Each separate stage of the experiment needs to be cropped and smoothed consistently to create an animation of the evolution of the topography. This step can be further analyzed using tools developed by Toenenboehn et al. (2018) to calculate the three-dimensional displacement and evolution of off-fault deformation.

points: 4,088,254
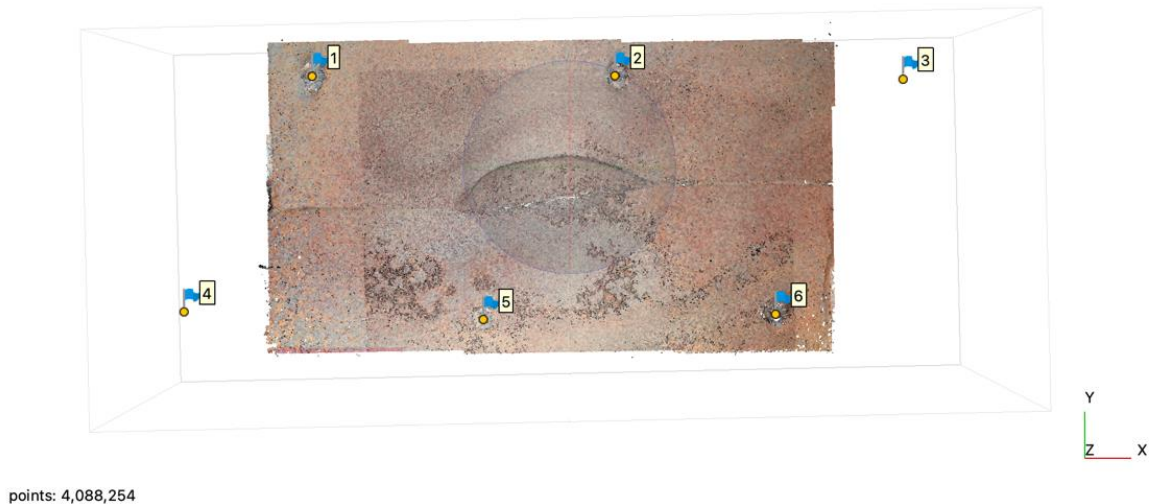
Figure 1.4: Final dense point cloud with over 4 million data points generated in Metashape. The blue flags and numbers indicate the position of the six control points placed on top of the surface of the clay. We cropped the raw dense point cloud to only show the area of interest. This dense point cloud represents the final stage of a 15° and 2 cm stepover restraining bend experiment.

To determine if this workflow provides sufficient resolution of the topography for our type of experiments and laboratory setup, I estimated the noise for each final surface

map. We determined that areas with patchy and uneven regions correspond to noise along

the surface of the claybox (Figure 1.5a). Transects along the patchy areas of the surface

map show the range of noise (small spikes) along each transect (Figure 1.5b). The noise

of the surface map is within ~1 mm, which guarantees fine-detail information of the

surface of the clay for experiments.
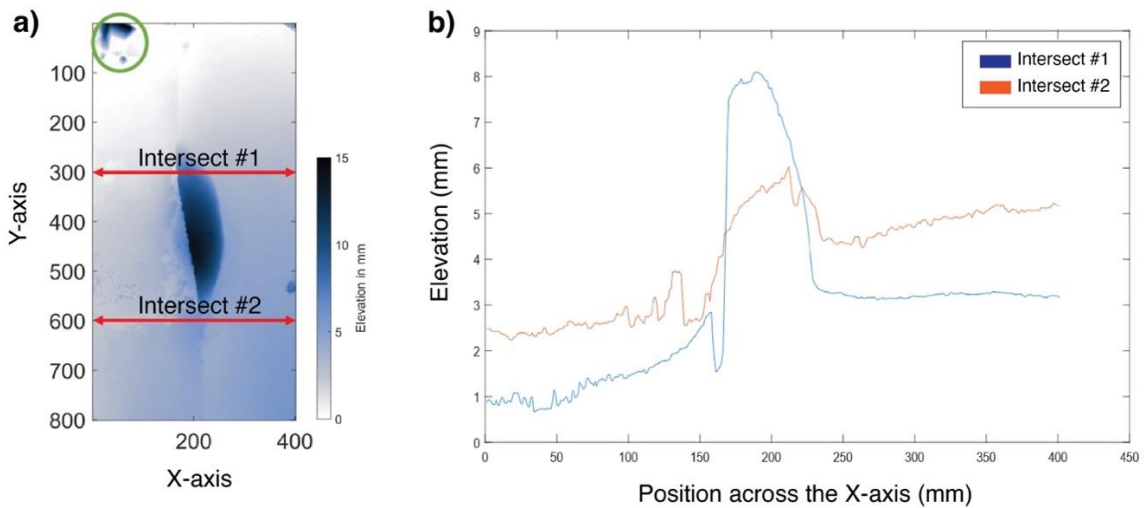
Figure 1.5: a) Surface map of 120 mm plate displacement of a 15˚ and 2 cm step over restraining bend experiment. Color bar indicates elevation of the surface measured in millimeters. Red arrows indicate the location of the transects across the noisy areas of the surface map to assess the magnitude of noise on the clay surface. Green circle captures the position of one of the 3D cylinders, which has a higher elevation than the rest of the clay surface. **b)** Blue line indicates first transect along row 300 and orange line indicates second transect along row 600. Note that both transects cut across the restraining bend (uplifted section) around 150 mm. Hence, the small spikes before the restraining bend represent the noisy area on the surface. The noise of the elevation profile stays under ~1 mm.

1.3 Results

I created a manual for the geomechanics laboratory on the best-practice workflow

that should be followed to optimize the elevation models. This process emerged after

many iterations and tests with different types of experiments. I used this workflow for 5

different strike-slip fault experiments (restraining bends and releasing bends) that had various basal conditions and loading rates configurations. The results from the releasing bend experiments, led by Alana Gabriel, are used in her paper currently in preparation to measure the dip of exposed normal fault surfaces – I am a co-author on that paper. Additionally, we designed four scripts that significantly speed up the process and, more importantly, achieve fine resolution of the surface of the wet kaolin during experiments. Our final surfaces generated have elevation uncertainty of $< \sim 1$ mm (Figure 1.5b) which guarantees accurate information of the topography of the clay. This accuracy of elevation models will allow us to quantify off-fault deformation manifested as advection and uplift/subsidence adjacent to strike-slip faults that evolve through time.

CHAPTER 2

THE IMPACT OF PRE-EXISTING WEAKNESSES ON STRIKE-SLIP FAULT EVOLUTION: RUPTURE MAPS FROM THE 2019 RIDGECREST EARTHQUAKE INSPIRE SCALED-PHYSICAL EXPERIMENTS

2.1 Introduction

The Eastern California Shear Zone of Southern California, USA, has hosted several historic ground rupturing earthquakes along complex networks of strike-slip faults. A contributing factor to the geometric complexity of these rupture traces is that they follow pre-existing faults and heterogeneities in the upper crust. For example, the 2019 Ridgecrest earthquake occurred in a region with pervasive pre-existing weaknesses that are at a high angle to the main rupture surface (e.g., Nevitt et al., 2023). The Ridgecrest earthquake produced a complex rupture pattern along the mainshock fault where the northwest end of the dextral rupture re-activated with sinistral slip a set of disconnected older faults perpendicular to the strike of the mainshock fault, also known as cross-faults (Figure 2.1; e.g., Antoine et al., 2021; Milliner et al., 2021). The highly segmented and disconnected geometry of active faulting at the northwest end of the rupture is believed to reflect very immature faulting that provides insights into the early development of strike-slip faults (Antoine et al., 2021; Milliner et al., 2021). Why did these NE striking sinistral faults re-activate rather than developing a new NW trending dextral fault that could accommodate the coseismic strain?

Understanding how the orientation of pre-existing cross-faults can influence the early evolution of strike-slip faults and strain localization over geologic time scales can inform future seismic hazard assessments of regions with pre-existing structures. Physical

experiments that simulate upper crustal deformation using scaled analog materials, such as wet kaolin, allow us to control loading and material rheology, and directly document the complete evolution of entire fault systems (Reber et al., 2020). Such temporal and spatial documentation of off-fault evolution is not possible from field data, which only offers a limited view of faulting patterns and shows the cumulative result of deformation. By tracking fault geometry and off-fault deformation during experiments of strike-slip fault evolution, we can gather information that can potentially guide interpretations of crustal faults.
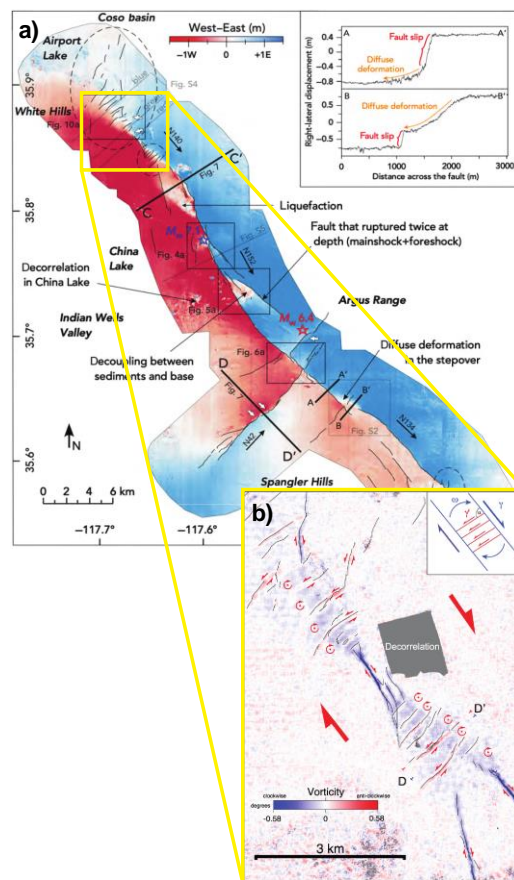
Figure 2.1: a) Ridgecrest's mainshock (epicenter marked by blue star) and foreshock (marked by red star) coseismic displacement map from Antoine et al. (2021). Transition to the Coso Basin on the northernmost section of the mainshock highlighted by yellow box. **b)** Closer look at the northeast trending faults with left-lateral slip shown with red (anti-clockwise vorticity) and right-lateral slip in blue (taken from Milliner et al., 2021).

2.2. Methods

Similar to many previous studies, we use wet kaolin as the analog material to conduct scaled physical experiments that simulate reactivation of slip along faults within the upper crustal (e.g., Bonini et al., 2016; Elston et al., 2022; Hatem et al., 2015; Henza et al., 2010; Toeneboehn et al., 2018; Bonini et al. 2023). Analog experiments that last a few hours in the laboratory give us the opportunity to directly observe and document processes that typically span thousands to a million years in the crust. We conducted scaled experiments within wet kaolin to simulate the initiation and maturation of crustal strike-slip faults with pre-existing weaknesses at a range of orientations.

2.2.1 Wet Kaolin Properties

This study uses a wet kaolin clay produced by the pottery industry as #6 tile clay. This kaolin rich material mostly consists of clay and silt particles, with a size less than 62 μm (Hatem et al., 2017) composed approximately 5-10% sand, 30-35% silt, and 60% clay-sized particles (Hatem et al., 2017). The high silt content provides low plasticity to the clay which facilitates localized faulting along sharp fault surfaces (Cooke & Van Der Elst, 2012). We use wet kaolin as the analog material because it produces localized and easy to track faults that are long-lived and pre-existing weaknesses can be introduced by cutting the clay (e.g., Bonanno et al., 2017; Bonini et al., 2023; Hatem et al., 2017). Furthermore, prior to failure, wet kaolin deforms as a bi-viscous Burger's material with both elastic and viscous properties that makes it well-suited to simulate inelastic crustal deformation processes at a variety of time scales (Cooke & Van Der Elst, 2012; Elston et

al., 2022). At failure, clay exhibits neutral rate and state frictional behavior that allow faults to constantly creep during experiments (Cooke & Van Der Elst, 2012).

To simulate crustal deformation processes in the laboratory, which is 5 orders of magnitude smaller than the crust, we need to scale the shear strength of the analog material to be five orders of magnitude weaker than the strength of the crustal material. We adjust the shear strength of the wet kaolin by modifying the water content. For instance, increasing the water content of the clay reduces the shear strength (Cooke & Van Der Elst, 2012; Eisenstadt & Sims, 2005). Hence, we modify the water content of the wet kaolin so that in situ fall cone strength test show undrained shear strengths of 119- 123 Pa for the experiments conducted in this study. The density of the wet kaolin used in the experiments discussed here is ~1.6 g/cm³ and the clay has a water content of 70-73% by weight. We collect samples of wet kaolin before and after each ~2 hours long experiment to assess changes in the water content. The water loss within the upper 1 cm is less than 3% for experiments discussed here, which correlates to only ~2 Pa increase in shear strength. The bottom half of the claypack does not experience water loss.

We follow the density and strength scaling relationship of the analog material and the crust employed by Henza et al. (2010) and used by previous studies (e.g., Cooke et al., 2013; Elston et al., 2022; Hatem et al., 2015, 2017) in which the strength (S) ratio of the model (m) to the prototype, or the crust, (p) is equal to the density (ρ) ratio of the model to the prototype multiplied by the length (Z) ratio of the model to the prototype:

$$\frac{S_m}{S_p} = \frac{\rho_m}{\rho_p} \frac{Z_m}{Z_p}$$

Using similar coefficients of internal friction for both the analog material and the Earth's crust (0.55-0.85; Henza et al., 2010; Reber et al., 2020), density of ρ_p= 2.65g/cm³ and strength of S_p= 10-20 MPa for the crust, and known density and strength of the analog material (Hatem et al., 2015), we determine that the length of 1 cm within the wet kaolin experiment is equivalent to 1-2 km in the Earth's crust.

The non-zero shear strength of the wet clay allows the introduction of planes of weaknesses by making cuts with an electrified probe into the clay prior to the onset of experiments. Upon deformation, the pre-cut surfaces may be reactivated before the failure of the intact clay (Reber et al., 2020). The ability of introducing planes of weaknesses into the analog material provides the opportunity of investigating fault evolution that incorporates deformation along existing weaknesses, such as other faults or bedding planes, in the crust (Bonanno et al., 2017; Bonini et al., 2016, 2023; Elston et al., 2022; Hatem et al., 2015, 2017).

2.2.1.1 Experimental Set-up

All strike-slip fault experiments are conducted using a split box apparatus (claybox) in which one half of the box remains static while the position of the other half is controlled by stepper motors that apply velocity of 0.5 mm/min in dextral slip at the basal boundary for all experiments discussed here (Figure 2.2). An overhead camera above the claybox captures images at 30 seconds intervals corresponding to 0.25 mm of applied displacement recorded per image. We emplace the claypack of 2.5 cm thickness

into the box from the center outward to prevent large air bubbles within the clay and

scrape the clay to produce a level surface.
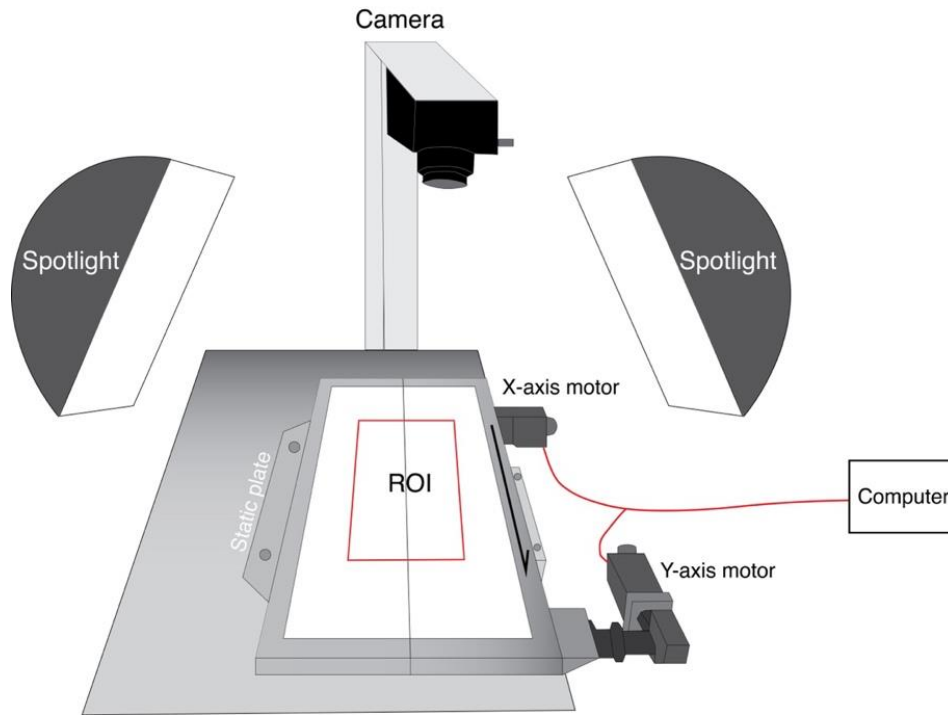
Figure 2.2: Laboratory set up for all localized basal shear strike-slip fault experiments where the plates are juxtaposed. Drawing depicts the claybox apparatus placed on a table top where one plate is attached to the table while the other plate moves via stepper motors with the prescribed velocity to impose dextral slip. Stepper motors are connected to a computer where we indicate the desired total displacement of the plate, the direction (X and/or Y-axis), and velocity in mm/min. Deformation within all experiments is documented with an overhead camera that takes photos at 30 seconds intervasl throughout the experiment. Spotlights with difussers provide even lighting while minimizing glare. Note the selected region of interest (ROI) for all experiments conducted in this study. This ROI was selected to avoid the boundary effects of the claybox apparatus. For distributed basal shear experiments we superglue a 1.5 cm wide elastic band on the bottom of each plate and pre-strech it to 2.5 cm prior to the onset of the experiment.

Following the preparation and placement of the clay into the split box apparatus,

we utilize a programmable plotter fitted with an electrified probe to create vertical

surfaces in the clay with the desired orientation and spacing. The small current in the probe reduces the drag of the probe through the claypack. After creating the weaknesses, we sieve red and black sand on the surface of the clay to provide contrasting texture for photos used for Digital Image Correlation, which generates incremental displacement fields from pictures taken throughout the experiment. The average image resolution for all experiments is around ~160 pixels/cm and we select the same region of interest for analysis for all plate-on-plate experiments and an enlarged region for elastic band experiments.

We vary three aspects of the experimental set up to assess the impact of various pre-existing weaknesses on strike-slip fault evolution. We vary both the initial orientation and spacing of the vertical surfaces, and we apply both localized and distributed basal shear. To create strike-slip fault experiments with localized basal shear we juxtapose both basal plates (Figure 2). For these experiments, we introduce planes of pre-existing weaknesses at initial angles of 60°, 90°, 120°, and 150° measures counterclockwise from the applied dextral shear orientation with spacings of both 2 cm and 5 cm.

For distributed basal shear experiments, we use a 1.5 cm wide elastic TheraBand™ glued to the bottom of the plates and pre-stretch to 2.5 cm prior to the onset of experiments to avoid ripping of the elastic band and undulations in the sheared TheraBand™. For experiments that include an elastic sheet between the basal plates, we introduce vertical surfaces oriented at 90°, 120°, and 150° with spacing of 2 cm. The experiments reach total displacement of 60 mm except for distributed basal shear experiments where the elastic band ripped prior to reaching 60 mm of plate displacement.

2.2.1.1.1 Data Processing

We utilize PIVlab 2.63 version for MATLAB (Thielicke & Stamhuis, 2014) to calculate the incremental displacement fields from the time series of overhead photos from each experiment. We adopt the multi-pass PIV workflow from Hatem et al. (2017), which analyses each image pair three times with a descending window size to refine the deformation field to yield data points every 12 pixels. This process results in displacement data every 0.75 mm. From the horizontal displacement field, we calculate the vorticity for each stage of the experiment, which reveals the localized fault slip and off-fault shear strain.

To detect faults from the incremental vorticity maps we follow the approach of Chaipornkaew et al. (2022) and use an adaptive threshold to create active fault maps for each stage of the experiment. The adaptive threshold detects faults from the stacked vorticity maps using a sensitivity of 0.1 and a neighborhood size that determines the region used to identify zones of localized high shear strain. For our study, we stack four consecutives strain maps to reduce random noise and use a neighborhood size of 5x5 mm2 to capture small fault details. After applying the adaptive threshold technique to detect areas of high incremental vorticity we apply a noise reduction filter to remove high shear strain regions with fewer than 8 connected pixels (area < 6 mm²) from the active fault maps.

Additionally, some experiments have random noise in low strain regions away from the fault zone, so we filter out these regions by eliminating noise in the top and bottom 15 rows of the fault map. The result of this step is a binary fault map with the active fault configuration from each stage of each experiment.

We can use the vorticity fields and active fault maps to assess the partitioning of strain as slip along faults and distributed deformation off of faults. From this assessment, we estimate the portion of applied velocity that is expressed as incremental slip along the active faults in the direction of the applied loading, called the kinematic efficiency (KE, e.g., Hatem et al., 2017). Hence, kinematically efficient faults have greater fault slip and less off-fault deformation (KE = 1 – off fault deformation). For this measure of kinematic efficiency, we only use the component of fault slip measured in the same direction as the applied velocity because we are interested in how the applied loading is partitioned on and off of faults. As faults propagate, link, and become throughgoing surfaces, their kinematic efficiency increases (e.g., Cooke et al., 2013; Hatem et al., 2017).

2.3 Results

All experiments with different basal boundary conditions, pre-existing weakness orientations, and spacings show the three stages of strike-slip fault evolution associated with strain localization defined by Hatem et al. (2017) for faults without pre-existing weaknesses. In the early stages of fault initiation, distributed shear strain started to localize along right-stepping echelon faults (Stage 1). With further deformation, these echelon faults reorganized through propagation, abandonment, and linkage (Stage 2) until they formed a continuous fault surface (Stage 3; Figure 2.3a-c).

The mechanical behavior, timing, and duration of these stages varied for initial orientation of the pre-cut surfaces, the spacing in between the surfaces, and the basal shear configuration. Some of the experiments also show an early phase of reactivation

prior to the development of new echelon faults. In addition to observing the reactivation of the pre-cut surfaces, we analyze the evolution of strike-slip faults with pre-existing structures by documenting the evolution of both kinematic efficiency of the fault system and the shear zone width.

2.3.1 Reactivation and Evolution of Fault Surfaces

Reactivation of pre-existing weakness occurred in experiments with surfaces at some but not all orientations. Experiments with pre-existing weaknesses oriented at 60˚ or 90˚ from the applied dextral shear direction did not show evidence of early slip along the surfaces in any of the experiments (Figure 2.3d and g, Figure 2.4d, and Figure 2.5a and d).

Instead, shear strain localized along new right-stepping echelon faults and the active fault network initiated similarly to the experiment with no pre-existing weaknesses (Figure 2.3a-b, 2.3d-e, 2.3g-h). In contrast, experiments with weaknesses oriented 120° from the applied shear reactivated with sinistral slip and experiments with weaknesses at 150˚ reactivated with early dextral slip in all experiments (Figure 2.3j and m, Figure 2.4g and j, and Figure 2.5g and j).

Localized Basal Shear with pre-cuts spaced every 2 cm

Evolution of pre-existing weaknesses

Early → Late
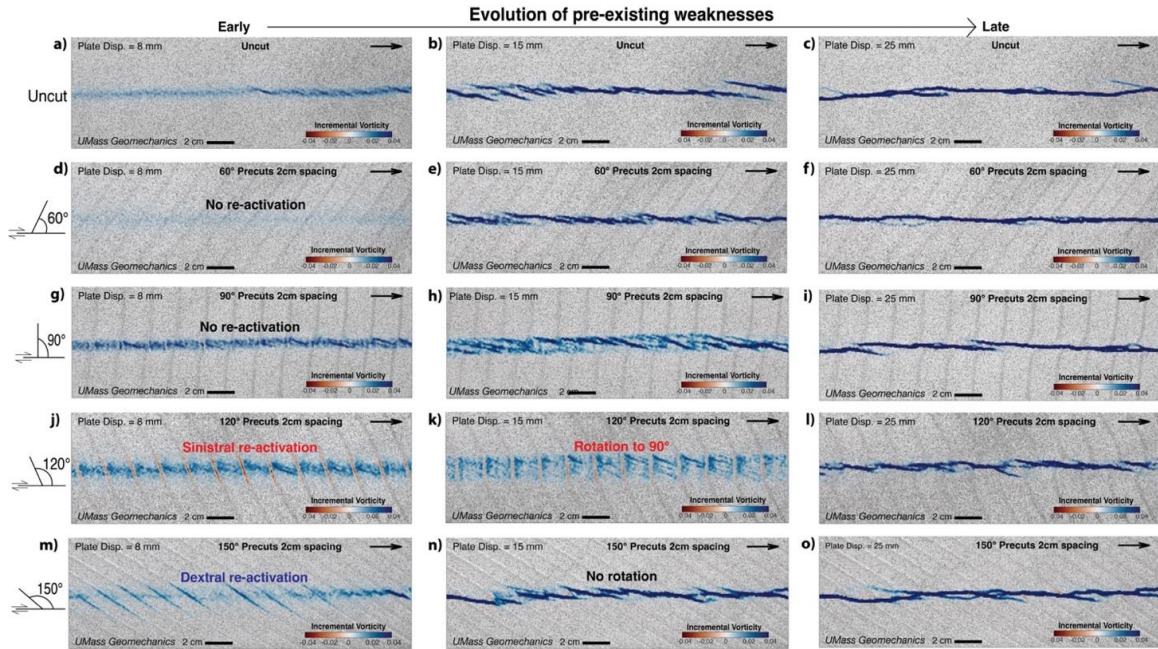
Figure 2.3: Incremental vorticity fault maps for localized basal shear experiments with **(a-c)** no pre-existing weaknesess, **(d-f)** with closely spaced pre-cut surfaces oriented 60° from the applied shear, **(g-i)** 90°, **(j-l)** 120°, and **(m-o)** 150°. (d-i) Experiments with pre-cut surfaces initially oriented between 60° and 90° showed no re-activation of the pre-existing weaknesess. (j-l) Experiments with pre-existing planes of weaknessess oriented 120° from the applied shear exhibited sinitral re-activation and clock-wise rotation. (m-o) Experiments with pre-cuts oriented 150° from the applied shear exhibited dextral re-activation with no rotation.

Distributed Basal Shear with pre-cuts spaced every 2 cm

Evolution of pre-existing weaknesses

Early → Late
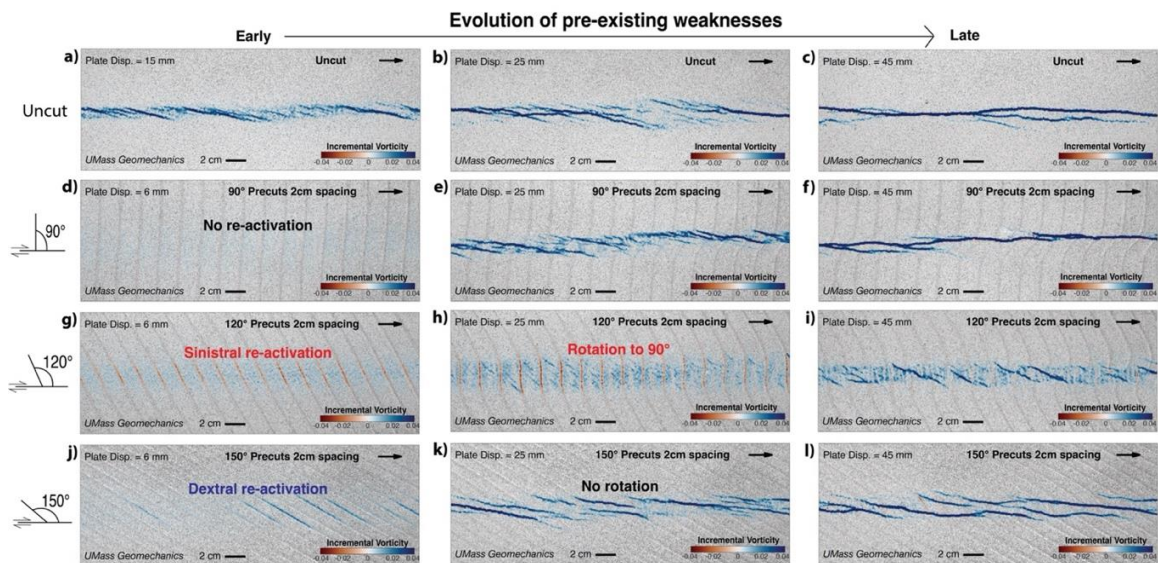
Figure 2.4: Incremental vorticity fault maps for distributed basal shear experiments with **(a-c)** no pre-cut surfaces, **(d-f)** with closely spaced pre-cut surfaces oriented 90°, **(g-i)** 120°, and **(j-l)** 150°. (d-f) Experiments with pre-existing surfaces initially oriented at 90° showed no re-activation of the pre-existing weaknessess. (g-i) Experiments with pre-existing planes of weaknessess oriented 120° from the applied shear exhibited sinitral re-activation and clock-wise rotation. (j-l) Experiments with pre-cut surfaces oriented 150° from the applied shear exhibited dextral re-activation with no rotation.

Localized Basal Shear with pre-cuts spaced every 5 cm
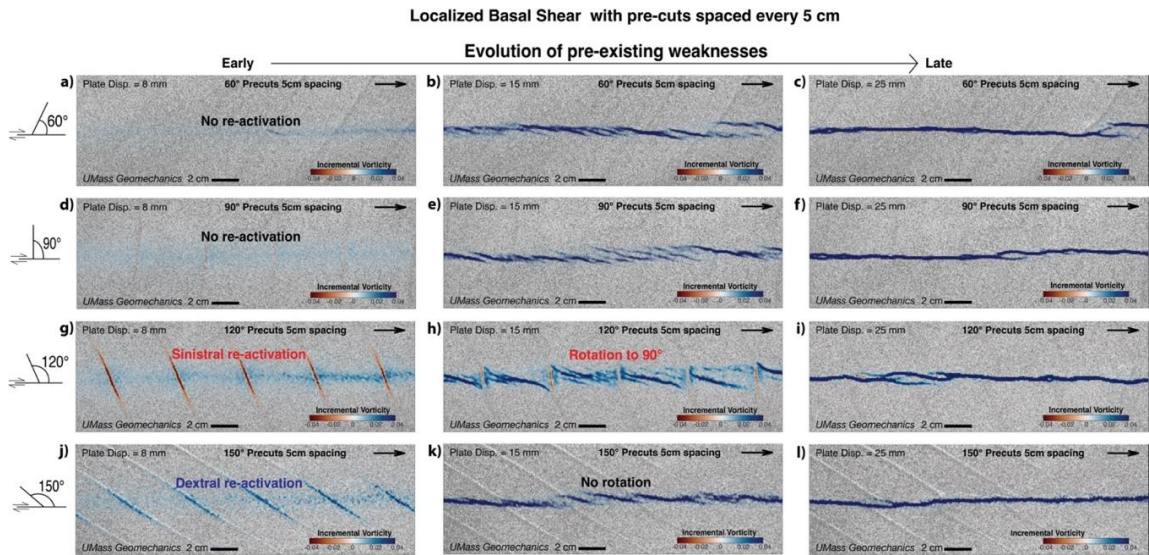
Figure 2.5: Incremental vorticity fault maps for localized basal shear experiments with widely spaced (5 cm) pre-cut surfaces oriented **(a-c)** 60° from the applied shear, **(d-f)** 90°, **(g-i)** 120°, and **(j-l)** 150°. (a-f) Experiments with pre-cut surfaces initially oriented between 60°and 90° showed no re-activation of pre-existing weaknessess. (g-i) Experiments with pre-existing planes of weaknessess oriented 120° from the applied shear exhibited strong sinitral re-activation and clock-wise rotation. (j-l) Experiments with pre-cuts oriented 150° from the applied shear exhibited dextral re-activation with no rotation.

Experiments with no pre-existing weaknesses, with 60°, and 90° pre-cut surfaces required almost the same amount of plate displacement to reach all three stages of strike-slip fault evolution and create a continuous strike-slip fault surface at 25 mm of plate displacement (Figure 2.3c, 2.3f, and 2.3i). In addition to the new echelon faults with similar spacing and orientation as in the uncut and 60˚ pre-cut surfaces experiments, the experiment with 90° pre-cut surfaces exhibited short-lived dextral slip that was limited to

the portions of the surfaces between the early echelon faults. This local reactivation

indicates that the presence of the 90° pre-cut surfaces impacted the reorganization of the

early echelon faults even if these surfaces were not reactivated at the start of the

experiment (Figure 2.3i).

For experiments with weaknesses oriented 120˚ from the applied shear direction,

the pre-cut surfaces developed short faults with sinistral slip that experienced significant

clockwise rotation during the experiments. In addition to localized sinistral slip along the

pre-cut surfaces, the early stages of the experiment showed distributed dextral shear

strain between the sinistral faults that contributes to the local rotation (Figure 2.3j, Figure

2.4g and Figure 2.5g). The sinistral faults that started oriented 120˚ from the direction of

shear rotated clockwise and continued to show sinistral slip until they were oriented ~90°

from the applied shear (Figure 2.3j-k, Figure 2.4g-h, and Figure 2.5g-h). Once the pre-cut

surfaces became perpendicular to the applied shear, the surfaces became inactive and

shear strain localized onto new dextral echelon faults located in between the pre-cut

surfaces. These new echelon faults propagated and linked and eventually formed a rough

localized slip surface without further reactivation along the pre-cut surfaces.

The experiments with pre-cut faults oriented 150˚ from the applied shear direction

showed early dextral slip but did not show rotation of slip surfaces documented in the

120˚ pre-cut surfaces experiments. After dextral reactivation of the 150° pre-cut surfaces

new dextral echelon faults with orientation closer to that of the applied shear (~165˚)

developed between the pre-cut surfaces. The 150˚ faults became inactive as the new

echelon faults propagated and linked to form a rough throughgoing surface with remnant

irregularities from the pre-existing weaknesses (Figure 2.3m-o, Figure 2.4j-l, and Figure 2.5j-l).

The amount of plate displacement needed to reach each stage of strike-slip fault evolution differed between the localized and distributed basal shear experiments with the same pre-cut surface orientations and spacings (Figures 2.3 and 2.4). For experiments with no precuts and surfaces that don't reactivate (e.g., 90˚), the distributed basal shear produces longer echelon faults than the experiments with localized basal shear (Figure 2.4b and e versus Figure 2.3b and h). Shear strain localized along new faults at around the same plate displacement for experiments with no pre-cut surfaces and with pre-cut surfaces that did not reactivate (e.g., 90°). On the other hand, distributed basal shear experiments needed 20 mm more of plate displacement than the localized basal shear experiments to obtain an almost thoroughgoing fault surface (45 mm versus 25 mm; Figure 2.3c and i, and Figure 2.4c and f). Additionally, the final fault surface for the distributed basal shear experiments showed a more segmented and rougher fault trace (Figure 2.4c and f) than that in the localized basal shear experiment (Figure 2.3c and i). Similarly, for experiments where pre-cut surfaces were reactivated (120° and 150°), the distributed basal shear experiments needed more plate displacement than the localized experiments for pre-cut surfaces to become inactive as strain localized on new echelon faults that eventually linked and formed a continuous fault surface (Figure 2.3j and m, Figure 2.4g and j).

Localized basal shear experiments with 5 cm wide pre-cut surfaces showed similar strike-slip fault evolution as the localized basal shear experiments with 2 cm pre-cut surfaces. Despite introducing wider spaced pre-cut surfaces into the wet kaolin, the

experiments did not need more plate displacement than the closely spaced pre-cut surfaces experiments to reach similar stages of strike-slip fault evolution (Figures 2.3 and 2.5). Experiments with non-reactivated cuts (90°) exhibited similar fault geometries at the same plate displacement for both pre-cut surface spacings (Figure 2.3g-i versus Figure 2.5d-f). Likewise, experiments with reactivated pre-cut surfaces (120° and 150°) had the same timing for reactivation, rotation (if present), abandonment of pre-cut surfaces, and localization of strain onto new echelon faults located in between the surfaces. Furthermore, we noticed that the final fault geometry of the widely spaced pre-cut experiments (Figure 2.5i and l) was smoother and more continuous that the equivalent closely spaced pre-cut experiments (Figure 2.3l and o) at the same plate displacement.

2.3.1.1 Partitioning of Strain as Pre-existing Weaknesses Evolve

To assess the distribution of fault slip and off-fault deformation as strike-slip faults with pre-existing weaknesses evolve, we track the kinematic efficiency to quantify the evolving mechanical behavior of faults (Figure 2.6). All experiments begin with 0% kinematic efficiency as the applied loading was accommodated as off-fault deformation and kinematic efficiency increases as the faults evolve and accommodate greater slip. Because the experiments with different precut surface spacing and basal loading evolve similarly, we only analyze the kinematic efficiency of experiments with 2 cm spacing between pre-cut surfaces with localized basal shear (Figure 2.3).
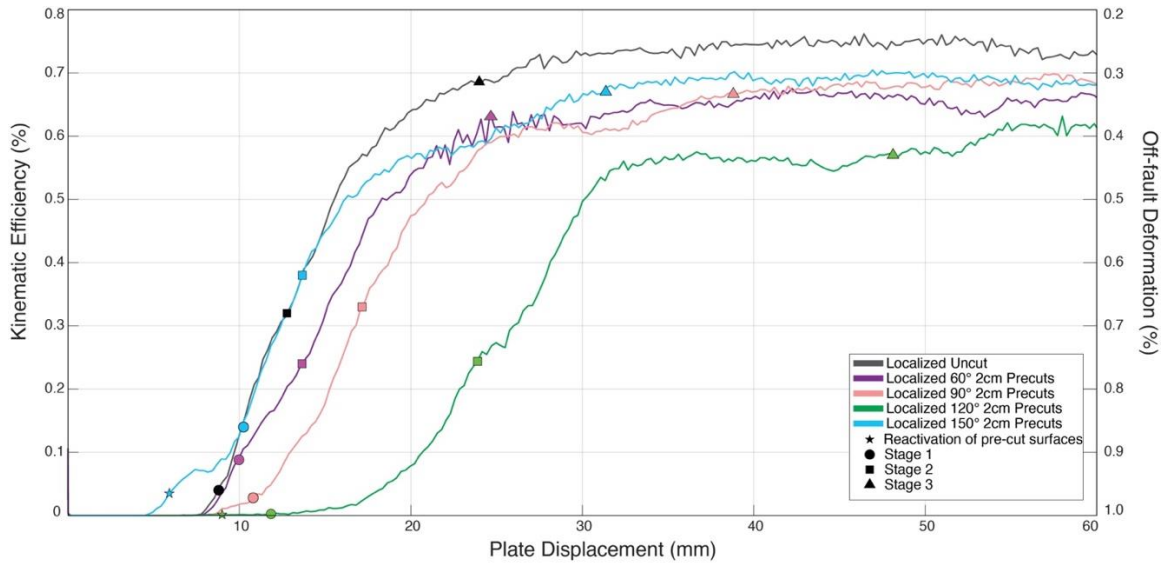
Figure 2.6: Kinematic efficiency versus plate displacement for all localized basal shear experiments with 2 cm spacing of pre-cut surfaces. The uncut experiment serves as a baseline for assessing the impact of the pre-existing weaknesses on strike-slip fault evolution. The symbols indicate the different stages of strike-slip fault evolution, and the star marks the reactivation of the pre-cut surfaces. Stage 1 is the early localization of shear along early echelon faults when faults first emerge. Stage 2 shows continued localization of strain as fault slip as echelon faults reorganize by propagation, abandonment, and linkage. By Stage 3 slip is localized along a continuous fault surface.

The evolution of kinematic efficiency for the uncut experiment serves as a baseline for assessing the impact of pre-cut surfaces on fault evolution. The kinematic efficiency started increasing in the uncut experiment with the emergence of the first right-stepping echelon faults at around 8 mm of plate displacement (Figure 2.6), followed by an increase in slip along the echelon faults as they started to propagate and reorganize at around 13 mm. At around 25 mm of plate displacement, when the fault developed a throughgoing surface, the kinematic efficiency for the uncut localized experiment approached 70%, indicating that 30% of applied deformation was distributed as off-fault deformation. As the fault continued to slip and become smoother, the kinematic efficiency increased close to 75% (25% off-fault deformation) and remained around that value for the rest of the experiment.

The uncut experiment has the highest kinematic efficiency from all experiments, indicating that even when pre-cut surfaces did not reactivate at the start of the experiment (60° and 90° surfaces), these pre-existing weaknesses contributed to the amount of off-fault deformation (Figure 2.6). The uncut, 60°, and 90° pre-cut surfaces experiments exhibited almost the same amount of plate displacement needed for the earliest emergence of faults (~10 mm) and the localization of strain on right-stepping echelon faults (~15 mm). At around 25 mm of plate displacement both the uncut and 60° pre-cut surfaces experiments exhibited a throughgoing fault surface with a kinematic efficiency of 68% and 63%, respectively. On the other hand, the experiment with 90° pre-cut surfaces required almost 15 mm more plate displacement to create a continuous fault surface with a kinematic efficiency of 66% (Figure 2.6). Despite the experiment with 90° pre-cut surfaces having great segmentation due to local short-lived reactivation of pre-cut surfaces during reorganization and needing more plate displacement to reach a continuous slip surface than the 60° experiment, the highest kinematic efficiency obtained by both experiments is almost 70%, indicating that once the continuous surface develops, strain partitioning on and off of the fault becomes stable. For these experiments without early reactivation of pre-cut surfaces, ~30% of the deformation is accommodated off of the mature fault (Figure 2.6).

The pre-cut surfaces oriented 120° from the applied shear direction had much lower kinematic efficiency than the other experiments. The 120° pre-cut surfaces reactivated with sinistral slip at around 8 mm but because of the orientation of this slip and the low slip rates, the component of right-lateral slip parallel to the loading direction remained low until after 10 mm of plate displacement (Figure 2.6). At 13 mm of plate

displacement the pre-cut surfaces became inactive, and strain started to localize on new right-stepping echelon faults with increased kinematic efficiency. The development of a suite of sinistral cross-faults early in the experiment promoted significant off-fault deformation, which is also manifested as clockwise rotation of material, including the faults, within the shear zone. Even after the 120˚ experiment developed a continuous slip surface at almost 50 mm of plate displacement, the off-fault deformation remains higher (~40%) than all other experiments (Figure 2.6).

The experiment with 150° pre-cut surfaces showed the earliest localization of fault slip and development of a fault system with high kinematic efficiency. The 150˚ experiment had an early bump in kinematic efficiency at around 5 mm of plate displacement when the pre-cut surfaces were reactivated with dextral slip. The dextral reactivation of the pre-cut surfaces suggest that they facilitated the early development of the strike-slip fault system compared to an uncut system. With further plate displacement, the emergence of new echelon faults that formed between the pre-cut surfaces around 10 mm of plate displacement increased kinematic efficiency to 15%. During the subsequent reorganization of the fault network kinematic efficiency reached almost 40%. With continued plate displacement, the fault generated a continuous slip surface after 30 mm of plate displacement with a kinematic efficiency of ~68%, indicating that 32% of the loading was partitioned as off-fault deformation. Despite the experiment having greater early fault slip than the uncut experiment, the presence of the 150° pre-cut surfaces increased the amount of off-fault deformation of the system resulting in kinematic efficiency values for the mature fault that are similar to those of 60° and 90° pre-cut surfaces experiments (Figure 2.6).

2.3.1.1.1 Evolution of Shear Zone Width

We follow the method used by Hatem et al. (2017) for calculating the evolution of the shear zone width using thresholds of the plate-motion parallel velocity. Along each transect across the fault network, we measured the distance between where the displacement at the surface of the clay reaches 20% and 80% of the applied basal plate velocity. We average the shear zone width from 446 transects across the fault and calculate the standard deviation (Figure 2.7a). We analyzed all localized basal shear experiments with closely spaced (2 cm) pre-cut surfaces to assess the impact of pre-existing weakness on the evolution of the shear zone width.
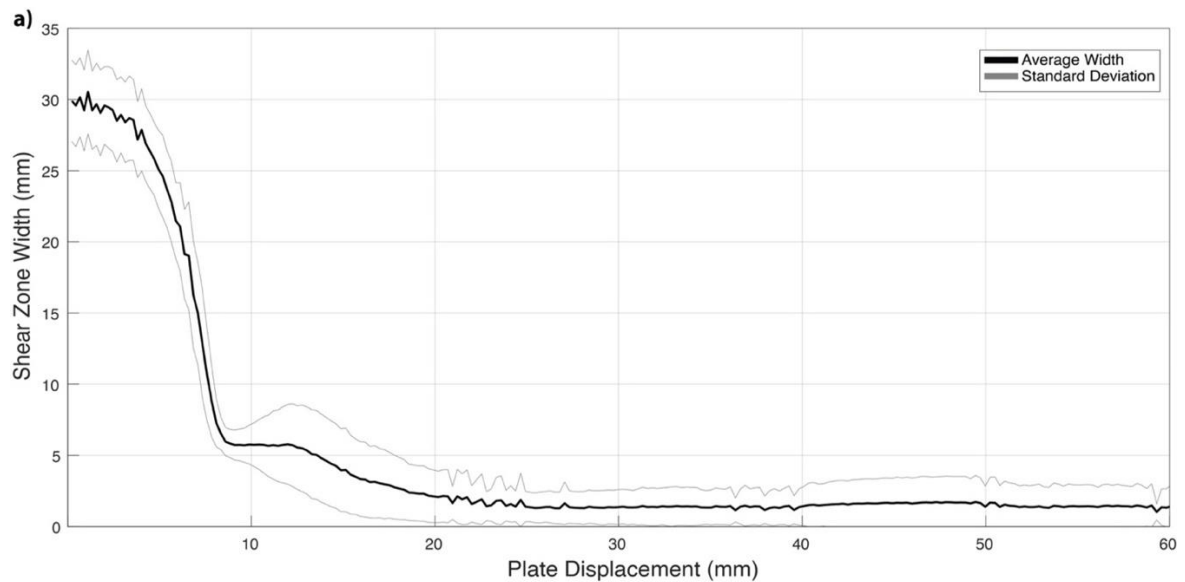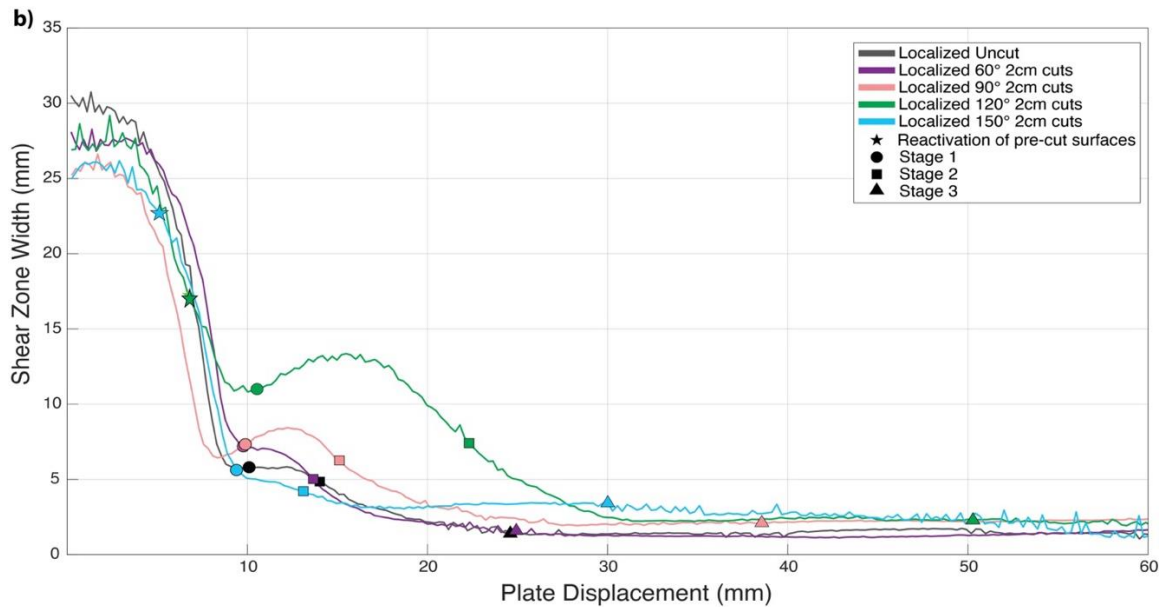
Figure 2.7: Evolution of shear zone width for experiments with localized basal shear. **a)** Evolution of shear zone width for experiment with no pre-existing weaknesses. Black solid line is the average width and grey solid lines show the standard deviation across the region of interest. **b)** Shear zone width for experiments with 2 cm spaced pre-cut surfaces oriented 60°, 90°, 120°, and 150° from the applied dextral shear and for experiment with no pre-existing weaknessess. The colored lines represent the average shear zone width for each experiment and the symbols indicate the onset of different stages of strain localization as strike-slip fault evolve (same symbols as Figure 6).

The experiments started with wide zones of distributed deformation and the width of the shear zones decreased nonlinearly with evolution of the strike-slip faults throughout all experiments (Figure 2.7b). The uncut experiment serves as the baseline for assessing the impact of pre-existing weaknesses on evolving shear zone width. In the uncut experiment, the shear zone width decreased within the first 10 mm of plate displacement with the emergence of the first faults at 10 mm (Figure 2.7b). As the new faults developed, the shear zone remained about 6 mm wide. As the early echelon faults started to propagate and reorganize at around 15 mm of plate displacement, the shear

43

zone width decreased until reaching a width of around 1.4 mm at the later stages of fault evolution (Figure 2.7b).

Experiments with surfaces oriented 60° and 90° from the applied shear direction showed similar shear zone width evolution to the experiment with no pre-existing weaknesses. The first few millimeters of plate displacement showed a continuous decrease of shear zone width until the earliest faults emerged at almost 10 mm of plate displacement for both experiments, after which the width remained ~7 mm wide for the 60° pre-cut surfaces experiment while the 90° experiment experienced a small increase in width to 8 mm. At 15 mm of placement, the 90˚ pre-cut surfaces briefly reactivated between the new echelon faults and contributed to a wider shear zone width compared to the 60° experiment (Figure 2.7b). Followed by the reorganization of echelon faults to generate a continuous mature fault surface at 25 mm of plate displacement for the 60° experiment and much later (38 mm) for the 90° experiment. The uncut and 60° experiment have a similar shear zone width of 1.4 mm when slip localized along a continuous and mature fault surface at 25 mm of plate displacement, whereas at 38 mm of plate displacement when there is a throughgoing slip surface for the 90° experiment, the shear zone width is higher (2.1 mm). The difference between plate displacement needed to generate a continuous fault surface in experiments with non-reactivated 90° surfaces (38 mm) and the uncut experiment (25 mm) indicates that the local and short-lived reactivation along these pre-existing weaknesses impacted the evolution of the shear zone width. The small difference in shear zone width between the uncut experiment and the experiment with 60˚ pre-cut surfaces that experience no reactivation is well within the standard of deviation for shear zone width.

The experiment with 120° pre-cut surfaces produced the widest shear zone during fault reorganization. The reactivation of the pre-cut surfaces at 7 mm of plate displacement was followed by a decrease in shear zone width as strain was accommodated along the pre-cut surfaces (Figure 2.3j). The increase in shear zone width at around 11 mm of plate displacement occurred as the pre-existing weaknesses rotated to ~90° from the applied shear direction. Because the length of each sinistral fault stayed the same during this rotation, the shear zone widened with rotation (Figure 2.3k). When the pre-cut surfaces became inactive at ~17 mm of plate displacement, the shear zone width decreased, and shear strain started to localize on dextral echelon faults that formed between the pre-cut surfaces. The shear zone width continued to thin as the echelon faults propagated, linked, and re-organized at 22 mm of plate displacement until reaching a final shear zone width of approximately 2.2 mm (Figure 2.7b).

The experiment with 150° pre-cut surfaces had a thinner shear zone width than the uncut experiment during the early stages of fault evolution but had thicker shear zone for mature faults. Because the 150˚ precut surfaces slipped before new faults developed in the uncut experiment (Figure 2.6), the reactivation of the pre-cut surfaces jumpstarted the strike-slip fault evolution. Consequently, the experiments with 150˚ pre-cut surfaces had a narrower shear zone than the uncut experiment between 10-15 mm of plate displacement (Figure 2.7b). Nonetheless, these planes of weaknesses impacted the shear zone width of the mature fault, which had wider shear zone width than the uncut experiment. At 15 mm of plate displacement, the fault system reorganized to form new echelon faults with shallower orientation than the pre-cut surfaces and the geometry of the new faults was impacted by the pre-cut surfaces. This reorganization contributes to

45

the increased segmentation of the mature fault in the 150˚ experiment compared to the uncut experiment and the wider shear zone width. The mature fault in the 150° pre-cut experiment has a similar mature fault shear zone width of around 2.1 mm to the 90° and 120° experiments that also had reactivation of the precut surfaces (Figure 2.7b). The wider shear zone for the mature faults that grow from even locally and ephemerally reactivated pre-cut surfaces may result from the geometric irregularities that they introduce that persist along the mature fault.

2.4. Discussion

2.4.1 Repeatability

To confirm the observations documented throughout each experiment, we ran a second suite of experiments with the same laboratory conditions as well as the wet kaolin recipe. We ran all localized basal shear experiments with closely spaced (2 cm) pre-cut surfaces twice per pre-cut surface orientation resulting in a total of 8 experiments (Table 2.1). Additionally, we conducted four localized basal shear experiments with widely spaced (5 cm) pre-cut surfaces at 60°, 90°, 120° and 150° from the applied shear. For distributed basal shear experiments, we ran three closely spaced pre-cut surfaces at initial orientations of 90°, 120°, and 150° (Table 2.1). Also, we ran experiments with no pre-existing weaknesses for both basal shear configurations to use as the baseline during our analysis and comparisons. In total, our study encompasses 17 strike-slip fault experiments with different basal shear conditions and variations in the orientation and

spacing of the pre-cut surfaces to document and assess the impact of pre-existing

weaknesses on strike-slip fault evolution.

We confirm that the findings presented here persist for each localized basal shear

experiment with closely spaced pre-cut surfaces. Experiments with 60° and 90° pre-cut

surfaces did not re-activate at the onset of the experiment, while all 90° experiments

exhibited local and short-lived reactivation of pre-cut surfaces during fault

reorganization. For the 120° experiments, the pre-cut surfaces reactivated with sinistral

slip and rotated to 90° from the applied shear whereas for the 150° experiments the pre-

cut surfaces reactivated with dextral slip but did not rotate.

2.4.1.1 Why Do Pre-existing Weaknesses at Various Initial Orientations Get Reactivated with Different Slip Senses?

Figure 2.8a shows a Mohr circle diagram schematically representing the stress

state within the early shear zone along with the slip envelopes required for 1) the

conditions for initiation of slip along pre-cut surfaces (black solid line) and 2) the

conditions for slip along surfaces that previously slipped and experienced some degree of

slip weakening (black dotted line). We also show pre-cut surface orientations with

reference to the applied shear direction, which is set up as the maximum shear direction

on the Mohr diagram.

Pre-cut surfaces orientated 60˚ and 90° to the applied shear direction have no

early reactivation and fall below the envelope for slip along pre-cut surfaces. On the other

hand, pre-cut surfaces at 120° from the applied shear showed strong sinistral re-activation

implying that the stress state is at (or exceeding) the threshold for sinistral slip (negative shear stress on Figure 2.8a) along these surfaces. Pre-existing surfaces at 150° from the applied shear showed dextral reactivation (positive shear stress on Figure 2.8a) indicating that the stress state meets (or exceeds) the threshold for slip along these surfaces. (Figure 2.8a).

The experimental results show that while pre-cut surfaces oriented at 90˚ to the applied shear direction did not slip, pre-cut surfaces oriented 120° from the applied shear that slipped and rotated to 90˚ did exhibit small sinistral slip (dashed arrows on Figure 2.8a). This observation is consistent with the inference that the threshold for slip along surfaces that have previously slipped, and consequently experienced slip weakening is lower than the threshold to initiate slip (Figure 2.8a). The process of accruing slip along the surfaces may align the clay particles and/or draw water to the fault zones that reduces its strength. By mapping the observations from the different experiments into the Mohr diagram, the claybox acts like an experimental rheometer to inform the properties of the clay.

We integrated the experimental results with previous findings of slip surface networks within the fault zone that use Riedel shear nomenclature (e.g., Davis et al., 2000). Figure 8b shows expected slip sense of pre-existing weaknesses with different orientations within a shear zone. We determined that pre-existing surfaces oriented anywhere between ~30°- 85° are likely to remain inactive as they are within the grey zone. Weaknesses oriented between ~85° - 135° from the imposed shear direction reactivate with sinistral slip, which is also supported by analysis of R' surfaces (e.g.,

Davis et al., 2000), and surfaces between ~145° - 185° exhibit dextral slip, which is

supported by analysis of R surfaces (e.g., Davis et al., 2000).
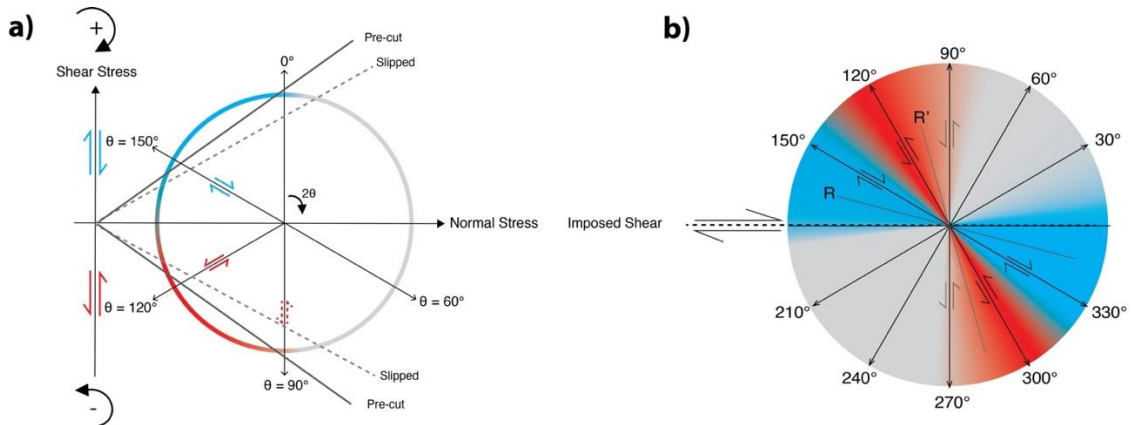
Figure 2.8: a) Schematic Mohr diagram depicting angles of orientation of pre-cut surfaces used in our study with circles for stress state within the shear zone. Color of the arrows indicate the sense of slip and dotted arrows indicate small amounts of slip. Failure envelopes show stress conditions for initial slip along the pre-cut surfaces ('pre-cut') and for surfaces that have previously slipped ('slipped'). **b)** Diagram of real world angle orientations for the pre-cut surfaces with expected sense of slip. R and R' indicate Riedel shear naming system used by many researchers.

2.4.1.1.1 What Do Strike-Slip Fault Experiments with Pre-existing Weaknesses Tell Us About the Faults that Hosted the 2019 Ridgecrest Rupture?

The northwest section of the Ridgecrest mainshock rupture is characterized by a

series of parallel, NE-trending sinistral faults that are orthogonal to the NW-trending

dextral faults (Figure 2.1b). This series of cross-faults are believed to predate the 2019

rupture and experienced re-activation during the Ridgecrest event. Previous studies that

analyzed the 2019 Ridgecrest rupture have proposed several reasons for the sinistral slip

of these cross-faults located northwest to the mainshock fault (Figure 2.1b). Milliner et al.

(2021) proposed that the left-lateral motion of the NE trending faults is mostly related to

individual block rotations inside the dextral shear zone of the northernmost section of the

mainshock rupture; this follows a 'bookshelf' faulting pattern proposed for many regions.

The bookshelf faulting occurs in two locations at either end of a NW-SE oriented dextral

fault (Figure 2.1b). In addition to bookshelf faulting, Antoine et al. (2021) have proposed

that these sinistral faults might be fingerprints of the rupture process because some of the

fault strands appear to be slightly curved or have a sigmoidal shape (Figure 2.1b). Others

have proposed that the dynamic stress pulse located ahead of the rupture tip triggered

motion along these pre-existing structures while the rupture was propagating towards the

north (Okubo et al., 2019). These proposed mechanisms are not exclusive of one another

as the same stress state can arise by multiple mechanisms. Regard of mechanism, we

propose that the reactivation of the high-angled pre-existing weaknesses located on the

northwest section of the Ridgecrest mainshock exhibited similar mechanical behavior and

evolution as the 120° pre-cut surface experiments conducted in our study. In the past, the

cross faults may have been oriented between ~135° and ~105° from the applied shear and

rotated clockwise to present-day orientation of the pre-existing structures within the shear

zone.

Studies by Milliner et al. (2021) and Antoine et al. (2021) demonstrated that the

series of parallel NE-trending faults have small sinistral slip while being oriented almost

perpendicular to the dextral mainshock fault. The present-day pattern of pre-existing

structures in the crust is similar to the experiments with pre-existing weaknesses oriented

120° from the applied shear at 15 mm of plate displacement. The experimental strike-slip

fault evolution suggests that these pre-existing structures might become inactive in the

future as strain continues to accumulate in the fault zone and may begin to localize on

new right-stepping dextral echelon faults. With continued deformation these echelon faults might propagate and link to create a mature throughgoing dextral strike-slip fault surface with remnant irregularities from the pre-existing structures.

2.5 Conclusion

Our study reveals that the presence of pre-existing weaknesses impacts the amount of off-fault deformation even if the weaknesses have limited and ephemeral reactivation. Experiments with limited reactivation of pre-cut surfaces (90°) had a higher degree of off-fault deformation than experiment with no pre-existing weaknesses (Figure 2.6). Experiments with significantly re-activated pre-cut surfaces (120° and 150°) also exhibited high amounts of off fault deformation. The experiment with 120° pre-cut surfaces had the highest degree of off-fault deformation due to the re-activation of a suite of sinistral cross-faults during early stages of fault evolution that lead to significant off-fault deformation, such as rotation of material including the cross-faults within the shear zone. The early reactivation also created irregularities that persisted along the continuous mature strike slip fault and contributed to off-fault deformation. The experiment with 150° pre-existing weaknesses exhibited a similar amount of off-fault deformation along the mature strike-slip fault to experiments with limited to non-reactivated pre-cut surfaces (60° and 90°) despite the early dextral re-activation of the surfaces that jump-started the earliest development of the strike-slip fault system. Hence, non-reactivated and re-activated pre-existing weaknesses impacted the amount of off-fault deformation of the system even after the continuous surface developed and deformation partitioning became stable.

The pre-existing structures on strike-slip faults also influenced the evolution of the shear zone width of the fault system. Our study demonstrated that experiments with 90°, 120°, and 150° pre-cut surfaces had a different shear zone width evolution than experiment with no pre-existing weaknesses or no reactivation (60° experiment). All three experiments had wider shear zones around the mature fault than the uncut and 60° pre-cut surfaces experiment due to the geometric irregularities that grew from the pre-cut surfaces and persisted throughout the evolution of the continuous fault surface.

We showed that laboratory experiments using crustal analog materials that are carefully scaled to simulate faulting deformation within the upper crust can shed insights on the impact and evolution of pre-existing weaknesses on strike-slip faults, like the 2019 Ridgecrest rupture. The findings from such experiments can be used to inform future seismic hazards of strike-slip faults with pre-existing weaknesses in the Earth's crust.

CHAPTER 3

PREDICTING OFF-FAULT DEFORMATION USING CONVOLUTIONAL NEURAL NETWORKS TRAINED ON EXPERIMENTAL STRIKE-SLIP FAULTS

3.1 Introduction

Surface offsets from strike-slip earthquake ruptures can underestimate the total slip at seismogenic depths because surface ruptures produce shallow distributed off-fault deformation in addition to localized slip (e.g., Milliner et al., 2021; Nevitt et al., 2020; Pollitz et al., 2020). This distributed strain within the upper 3-4 km (Kaneko & Fialko, 2011), can manifest as secondary faulting and/or pervasive continuous shear (Milliner et al., 2021). The degree and nature of off-fault deformation depends both on the rock and soil properties and the geometry of the primary slip surface (e.g., Milliner et al., 2021; Nevitt et al., 2020). For example, smooth and continuous strike-slip faults can more efficiently accommodate slip with less off-fault deformation than faults with more rough or segmented traces in the slip direction (e.g., Chester & Chester, 2000; Fang & Dunham, 2013; Newman & Griffith, 2014; Saucier et al., 1992).

The hypothesis that smoother faults produce greater slip is strongly supported by scaled physical experiments that simulate the evolution of strike-slip faults (Hatem et al., 2017; Visage et al., 2023). The direct and complete observations available from laboratory experiments provide insights not available from field data, which generally reveal only cumulative deformation and parts of the fault structure (e.g., Reber et al., 2020). The power of scaled experiments derives from using carefully controlled analog materials that simulate within the laboratory, the same deformation processes that act

across kilometers and thousands of years in the upper crust. Scaled physical experiments that simulate crustal strike-slip fault development with a range of analog materials, loading rates, and boundary conditions reveal the evolution of both active fault networks and off-fault deformation values that are consistent with field measurements of crustal faults (Hatem et al., 2017; Lefevre et al., 2020; Visage et al., 2023). Additionally, deep learning can use the rich results from physical experiments to build Convolutional Neural Networks (CNN) that can estimate off-fault deformation from maps of active faults (Chaipornkaew et al., 2022). CNN are supervised deep learning algorithms capable of extracting features and accurately recognizing patterns in input images.

In this study, we build upon the CNN developed by Chaipornkaew et al. (2022) and use the experimental time series of active fault maps generated from strike-slip fault experiments in three different materials to train and test CNNs to predict off-fault deformation. By including a range of analog materials that reproduce upper crustal deformation processes (wet kaolin, poured sand and sieved/sedimented sand), the CNN can capture a wide range of processes that contribute to the crustal shallow slip deficit. Furthermore, the experiments include a variety of loading rates and basal conditions to simulate a wide range of crustal conditions that may control evolution of both fault geometry and off-fault deformation. Using experimental strike-slip fault datasets, we train the CNN to associate the geometry of the active fault networks with the degree of off-fault deformation. We test each trained CNN on experimental fault maps produced within different materials, on synthetic fault maps, and on crustal strike-slip fault maps of different maturity for which we have estimates of off-fault deformation. Because the CNNs are trained on analog experiments that are carefully scaled to simulate upper

crustal deformation, they can be used to estimate off-fault deformation and shallow slip

deficit for crustal faults that are similar to those in the experiments. With this approach,

the trained CNN may provide estimates for the potential shallow slip deficit along crustal

faults that do not currently have sufficient information on off-fault deformation and these

estimates can contribute to seismic hazard assessment.

3.2 Scaling and Rheology of Analog Materials

Wet kaolin and dry sand have previously been used as analog materials for crustal

deformation because they both replicate brittle failure and localized deformation of the

upper crust (e.g., Eisenstadt & Sims, 2005; Reber et al., 2020). For instance, wet kaolin

deforms viscoelastically followed by frictional failure with the formation of localized

faults (Reber et al., 2020) (Figure 3.1a). On the other hand, dry sand demonstrates

distributed plastic deformation upon loading associated with the rearrangement of

granular force chains followed by localized frictional failure (Figure 3.1c and d; Panien et

al., 2006; Rudolf et al., 2023). The materials differ in the nature of distributed

deformation prior to failure, but both exhibit shear weakening upon the formation of

localized fault surfaces and have similar coefficient of internal friction to crustal

materials (Eisenstadt & Sims, 2005). The difference in distributed deformation prior to

failure on wet kaolin and dry sand may impact the off-fault deformation that develops

near strike-slip faults.

To simulate upper crustal deformation processes in the laboratory with

apparatuses that are five orders of magnitude smaller than the Earth's crust, we need to

adequately scale the strength of the analog material to also be five orders of magnitude weaker than the strength of the crustal material. The density and strength scaling relationship of the analog material and the crust is:

$$\frac{S_m}{S_p} = \frac{\rho_m}{\rho_p}\frac{Z_m}{Z_p}$$

in which the strength (S) ratio of the model (m) to the prototype (p) is equal to the density (ρ) ratio of the model to the prototype multiplied by the length (Z) ratio of the model to the prototype (e.g., Cooke et al., 2013; Hatem et al., 2015, 2017; Henza et al., 2010; Hubbert, 1937).

Both analog materials and the crust have similar coefficient of internal friction (0.55-0.85; Henza et al., 2010; Panien et al., 2006; Reber et al., 2020). Using a density of ρ_p= 2.65g/cm³, and a strength of S_p= 10-20 MPa for the Earth's crust (Hatem et al., 2015), we determine that the length of 1 cm within the wet kaolin experiment is equivalent to 1-2 km of the crust and 1 cm in the sand box represents 2 km in the Earth's crust (Table 3.1; e.g., Elston et al., 2022; Hatem et al., 2015; Lefevre et al., 2020; Visage et al., 2023).

All strike-slip fault experiments with wet kaolin have a thickness of 2.5 cm that scales to 1.9-3.5 km of crustal material and the sand pack thickness in experiments with dry sand ranges from 2.5-7 cm that scales to 5-14 km in the crust. Within the crust, slip at 3-4 km depth decreases towards the surface due to the shallow slip deficit (e.g., Kaneko & Fialko, 2011). Thus, the thicknesses of the experimental claypack and sandpack scale to the crustal thicknesses over which we detect the shallow slip deficit.
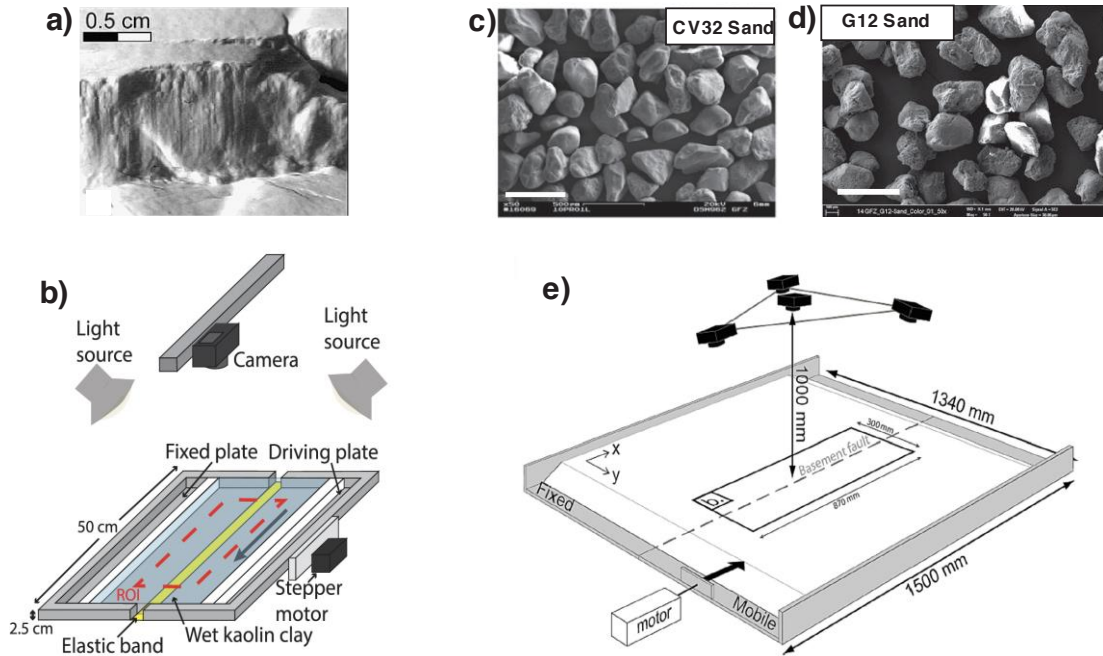
Figure 3.1: **a)** Image of a normal fault surface on wet kaolin taken from Henza et al. (2010) showing fine slickenline features. **b)** Schematic diagram of experimental set up for experiments on wet kaolin taken from Chaipornkaew et al. (2022). Split box set up illustrates distributed basal shear configuration with elastic band between the plates. For localized basal shear, the plates are juxtaposed. **(c-d)** Granular dry sands used for strike-slip fault experiments (Klinkmuller et al., 2016). **c)** CV32 denotes the Fontainebleau aeolian quartz sand used for experiments that train and test the CNN and d) G12 is the quartz sand to test the CV32 trained CNN. **e)** Experimental set up for strike-slip fault experiments in dry sand modified from Visage et al. (2023).

Table 3.1: Physical properties of analog materials used for strike-slip fault experiments (Klinkmüller et al., 2016; Reber et al., 2020; Rudolf et al., 2023; Visage et al., 2023).

Analog Material	Composition (wt%)	Mean Grain Size (μm)	Bulk Density (g/cm³)	Peak static friction coefficient	Length scaling
Wet Kaolin	5-10% Sand, 30-35% Silt, 60% Clay	62	1.6	0.7	1 cm = 1-2 km
Poured Sand CV32	98% Quartz	250	1.68	0.66	1 cm = 2 km
Sedimented Sand CV32	98% Quartz	250	1.71	0.96	1 cm = 2 km
Sieved Sand G12	95% Quartz	271	1.53	0.86	1 cm = 1-10 km

3.2.1 Wet Kaolin Rheology

Prior to failure, wet kaolin behaves as a bi-viscous Burger's material with both elastic and viscous deformation that makes it well-suited to simulate crustal deformation at a variety of time scales in the Earth's crust (Cooke & Van Der Elst, 2012; Elston et al., 2022). After failure, wet kaolin exhibits neutral rate and state frictional behavior so that the experimental faults exhibit creep (Cooke & Van Der Elst, 2012).

Numerous studies have successfully utilized wet kaolin clay to simulate fault evolution under extension, shortening, strike-slip, and inversion of the Earth's crust (Bonini et al., 2016, 2023; Cooke et al., 2013; Eisenstadt & Sims, 2005; Elston et al., 2022; Hatem et al., 2015, 2017; Henza et al., 2010; Toeneboehn et al., 2018; Withjack et al., 2007). The wet kaolin used for the analog experiments performed at the University of Massachusetts Amherst is produced for the pottery industry and sold as #6 tile clay (Figure 3.1a; Cooke & Van Der Elst, 2012). It is mostly composed of clay and silt size particles less than 62μm (Hatem et al., 2017; Reber et al., 2020). The high silt content of the kaolin type clay provides low plasticity index of 9-10 that facilitates localized faulting (Cooke & Van Der Elst, 2012). Additionally, the non-zero shear strength of wet kaolin facilitates continued slip along non-optimally oriented fault surfaces rather than continuous development of new fault surfaces (e.g., Cooke & Van Der Elst, 2012; Eisenstadt & Sims, 2005; Henza et al., 2010).

We modify the shear strength of the wet kaolin by altering the water content in order to scale the clay to the Earth's crust (e.g., Cooke & Van Der Elst, 2012; Hatem et al., 2017). Increasing the water content of the clay reduces the shear strength (Cooke & Van Der Elst, 2012; Eisenstadt & Sims, 2005). We modify the water content of the wet

kaolin so that in situ fall cone strength tests show undrained shear strengths of 100-107 Pa (Chaipornkaew et al., 2022). The shear strength of the wet kaolin depends on loading rate so that the 100-107 Pa measured in the relatively fast fall cone test corresponds to about 55-65 Pa at the 0.25-1.5 mm/min that we load the experiments. The wet kaolin discussed here has a density of ~1.6 g/cm³ and water content of 71-77% by weight (Table 3.1). We also collect samples of wet kaolin before and after the several hours long experiments to assess changes in the water content. The water loss in the upper 1 cm of the clay is less than 2% during experiments and correlates to only around 2 Pa increase in strength. The lower half of the claypack does not change in water content during the experiments.

3.2.1.1 Dry Sand Rheology

Quartz sand is widely used for modeling the brittle deformation of the upper crust due to its ease of use and dynamic scalability to the Earth's crust (e.g., Reber et al., 2020). The analog experiments discussed here utilize two dry sands from different laboratories. The coarse, well-sorted, Fontainebleau aeolian quartz sand (CV32) used at the University of Cergy has 98% quartz with a mean grain size of 250 μm (Figure 3.1c; Visage et al., 2023). A second angular, well-sorted quartz sand (G12) used at GFZ Potsdam has 95% quartz with a mean grain size of 271 μm (Figure 3.1d; Klinkmüller et al., 2016; Rudolf et al., 2023).

We train and test the CNN on data from strike-slip faults that evolve within the poured and sedimented CV32 sand. Subsequently, we use the CNN trained on CV32 to

test on the two G12 sand experiments to assess the predictive power of CNN on similar sand not seen during training.

Dry sand undergoes strain-hardening prior to failure followed by strain-weakening at the onset of faulting (Cubas et al., 2010; Eisenstadt & Sims, 2005; Klinkmüller et al., 2016; Lohrmann et al., 2003; Maillot, 2013; Panien et al., 2006; Rudolf et al., 2023). Just prior to developing localized faults the sand develops arrays of short-lived shear bands in the region of incipient faulting (Dotare et al., 2016; Lohrmann et al., 2003; Panien et al., 2006; Visage et al., 2023). In order to accommodate shear within these bands the sand pack dilates as individual grains adjust to move past one another. The dilatant nature of early faulting in sand experiments depends on the grain size of the sand and the nature of sand grain packing.

Previous studies demonstrated that the properties of sand depends on whether the sand is sedimented, sifted, or poured (Klinkmüller et al., 2016; Lohrmann et al., 2003; Maillot, 2013; Panien et al., 2006). Sedimented and sifted sand packs will generate more densely packed grains with higher internal friction coefficients that require more dilatancy to create faults (Lohrmann et al., 2003; Maillot, 2013; Panien et al., 2006; Rudolf et al., 2023).

Whereas, poured sand packs produce under-compacted sand grains with lower internal friction coefficients and lesser dilation upon shearing (Table 3.1; Visage et al., 2023). The significant dilation associated with early faulting within sedimented or sifted sandpacks may not replicate the most common processes of crustal faulting (Eisenstadt & Sims, 2005; Visage et al., 2023).

3.3 Methods

3.3.1 Experimental Set up

All strike-slip fault experiments performed at the laboratories of the University of Massachusetts Amherst, the University of Cergy, and GFZ Potsdam use a split box apparatus in which one half of the box remains static while the other half is controlled by a stepper motor that applies either dextral (clay and G12 sand experiments) or sinistral (CV32 sand experiments) slip at the basal boundary (Figure 3.1b and e). For presentation purposes, we flip the CV32 experiments results so that all experiments show similar slip sense.

To simulate a range of strike-slip loading styles, the experiments have various basal shear conditions (i.e., basal friction and localized or distributed shear) as well as different loading velocities. The clay experiments are the same as those reported in Chaipornkaew et al. (2022) and the CV32 sand experiments are reported by Visage et al. (2023) and Lefevre et al. (2020). The G12 sand experiments are new to this study.

Strike-slip fault experiments with wet kaolin include distributed shear over a 2.5 cm elastic band secured between the basal plates and localized shear above juxtaposed plates. Both sets of experiments have prescribed loading rates of 0.25, 0.5, 1.0, and 1.5 mm/min. Chaipornkaew et al. (2022) conducted each experiment configuration twice, resulting in a total of 16 dextral strike-slip fault experiments with variations of basal shear and loading rates (see Table S1 in appendix).

The strike-slip fault experiments with CV32 dry sand performed by Visage et al. (2023) and Lefevre et al. (2020) use a range of sand pack thicknesses, friction of basal

materials, and deposition techniques (e.g., sedimented and poured). The sedimented sand was deposited over a basal discontinuity using a sedimentary device that ensures uniform density of the sand pack (Maillot, 2013). For poured sand experiments, the sand was manually deposited with small increments while using a squeegee to smooth the surface (Lefevre et al., 2020; Visage et al., 2023). For this study, we use 32 strike-slip fault experiments with sedimented sand and 18 experiments with poured sand with sand pack thicknesses ranging at 2-7 cm and basal materials that include PVC (polyvinyl chloride), sandpaper, and alkor-foil (Lefevre et al., 2020; Visage et al., 2023) (see table S2 in appendix).

We excluded from our analysis strike-slip fault experiments thinner than 2.0 cm and 2.5 cm with sedimented and poured sand respectively because thin sandpacks do not produce early echelon faults upon shearing. Strike-slip fault experiments with thin sand packs produce smooth continuous faults without significant fault geometry variability (Lefevre et al., 2020) needed for CNN training. We also excluded experiments with sandpacks thicker than 7 cm because these experiments generate 3 or fewer fault maps (explanation in section 3.3.1.1.1), which does not allow us to split the dataset into independent sets for training, evaluating, and testing of the convolutional neural networks.

We use two strike-slip fault experiments with G12 dry sand from the GFZ Potsdam Laboratory. The G12 sand experiments were sieved onto alkor foil covered basal plates creating 3 cm thick sandpacks. The stepper motors displaced half of the split box at 6 mm/min.

3.3.1.1 Digital Image Correlation

All experiments use Digital Image Correlation from a series of photos taken with an overhead camera to document the surface deformation. During experiments with wet kaolin, the overhead camera captured images every 0.3 mm of basal displacement (Chaipornkaew et al., 2022). Overhead images were taken every 0.5 mm of basal displacement for experiments on CV32 sand (Lefevre et al., 2020; Visage et al., 2023) and every 0.1 mm/min during G12 sand experiments. We select a region of interest to avoid boundary effects of the split box for all experiments.

The G12 and CV32 sand include dyed grains to facilitate the correlation of pixels between successive photos. Similarly, prior to the onset of the clay experiments red and black sand is sieved on top of the wet kaolin to provide contrasting texture to facilitate the Digital Image Correlation (e.g., Hatem et al., 2017; Chaipornkaew et al., 2022). We employ Digital Image Correlation using Particle Image Velocimetry (Thielicke & Stamhuis, 2014) to determine the incremental horizontal displacement fields from successive images taken throughout the duration of the experiment (e.g., Adam et al., 2005).

3.3.1.1.1 Preparing Fault Maps and Label for Training and Testing the CNN

The training of the CNN requires both active fault maps (binary 64 x 128 pixel maps) and off-fault deformation data (label) from the experiments. We develop the active fault maps and label data needed to train the CNN from time series of the incremental horizontal displacement maps. A median filter reduces noise in the incremental

displacement fields while preserving displacement discontinuities along fault segments without introducing smearing. The vorticity and divergence of the incremental horizontal displacement fields provide the shear and dilatational strain respectively that can be summed to inform the net incremental strain for each stage of the experiment.

The active fault maps for each stage are the regions of the incremental net strain map with localized strain higher than the background. We detect the faults from the background strain using an adaptive threshold also used in Chaipornkaew et al (2022). However, before we can apply the adaptive threshold to the incremental strain maps, we have to scale all of the displacement fields so that each 64 x 128 pixel fault map window from every experiment includes comparable portions of the fault network. For example, we would not want 64 x 128 pixel fault maps from one experiment to include many early echelon fault segments while 64 x 128 pixel fault maps from another experiment with higher resolution photos only show a smooth portion of one fault trace without capturing nearby segments.

To produce comparable active fault maps, we tailored the down-sampling of the incremental displacement fields for each experiment so that each 64 x 128 pixel fault map window captures about three early echelon faults. Using this approach, each fault map window will be wide enough to completely span at least one stepover between early echelon strike-slip faults. Because the early segmented echelon faults develop differently within different analog materials and because thicker material above the basal plates produces wider spaced echelon faults (e.g., Hatem et al., 2017; Lefevre et al., 2020), the physical width represented in fault map windows differs between experiments.

While Chaipornkaew et al. (2022) used fault map windows that were twice as wide as the typical echelon spacing in the wet kaolin experiments, in this study, we widen the windows to three times the typical echelon length to better ensure that the fault maps in each window completely capture stepovers. Because all clay experiments have 2.5 cm thickness and early echelon fault spacing of ~3.6 cm, we use a fault map window width of 11 cm and down sample the wet kaolin experimental displacement fields so that 64 pixels equals 11 cm. For dry sand experiments, the early echelon fault spacing depends on sand pack thickness, whether the sand is sedimented or poured, and the basal friction material (Lefevre et al., 2020).

We use the empirical correlations developed by Lefevre et al. (2020) for the inter-echelon spacing for the CV32 sand experiments to estimate the appropriate fault map window width. For the G12 sand experiments, we use the empirical relationships developed by Lefevre et al. (2020) for sedimented CV32 sand. For each experiment, the displacement fields are down-sampled so that each 64 pixel wide fault map window spans three echelon spacing. The resulting window widths ranges from 8 - 50 cm for the sedimented sand and 12 - 28 cm for poured sand experiments (see table S2 in appendix).

Robust training of the CNN requires many independent active fault maps. To increase the number of windows per experiment, we allow up to 50% overlap of fault map windows. Thicker experiments generally require greater overlap than thinner experiments to optimize the number of windows per experiment stage (Figure 3.2). The overlap ranges from 20% to 50% within all experiments (see table S1 and S2 in appendix).
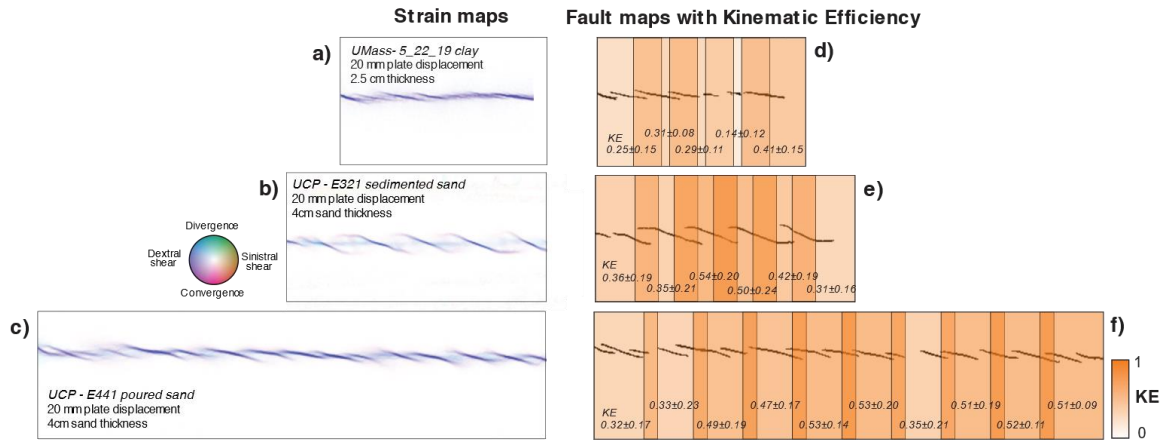
Figure 3.2: (a-c) Incremental strain maps for wet kaolin, sedimented sand, and poured sand representing 20 mm of plate displacement and varying thicknesses. Hue indicates sense of strain while saturation indicates amount of strain. Faults in wet kaolin show mostly shear within a localized fault zone whereas faults in sedimented sand have distinct dilation and convergence during early stages of fault evolution. Early faults in poured sand have similar geometric patterns to faults in wet kaolin. **(d-e)** Fault maps generated from stacked net strain stages. We generate fault map windows that span a stepover between the echelon faults and have window overlaps depending on clay and sand pack thicknesses. We also generate the kinematic efficiency labels that will be used for training and testing the convolutional neural network.

From the down-sampled incremental horizontal displacement fields, we calculate

the incremental vorticity, divergence, and net strain to detect active faults (Figure 3.2).

We calculate the incremental net strain by adding the absolute values of the incremental

vorticity and divergence maps and stack the incremental net strain over 5 stages to reduce

noise. The adaptive threshold technique used by Chaipornkaew et al. (2022) detects faults

from the stacked net strain maps using a sensitivity of 0.1 and a neighborhood size that

determines the region used to identify zones of localized high strain. When using a small

neighborhood size, the adaptive threshold only detects regions with the highest strain

resulting in few and thin faults (Figure 3.2b).

On the other hand, a high neighborhood size generates fault maps with thick and

overly connected faults (Figure 3.2c). While experimental fault zones have similar width,

due to the variable down-sampling of the incremental displacement maps, using the same

neighborhood size for all experiments would produce fault maps that have large variations in fault trace thickness. To prevent the CNN from training on fault maps with variable fault trace thickness, each experiment has a neighborhood size that yields fault traces with thicknesses between 2-4 pixels (see tables S1 and S2 in appendix).

Consequently, experiments with small down-sampling ratios use large neighborhoods (9x9 pixels) to detect small fault details while experiments with high down-sampling ratios use a small neighborhood size (5x5 pixels) to avoid wide and overly connected faults. Overall, a 7x7 pixels neighborhood works well for most experiments in wet kaolin and dry sand with the exceptions made for sand experiments with very low or high down-sampling ratios (see table S2 in appendix).
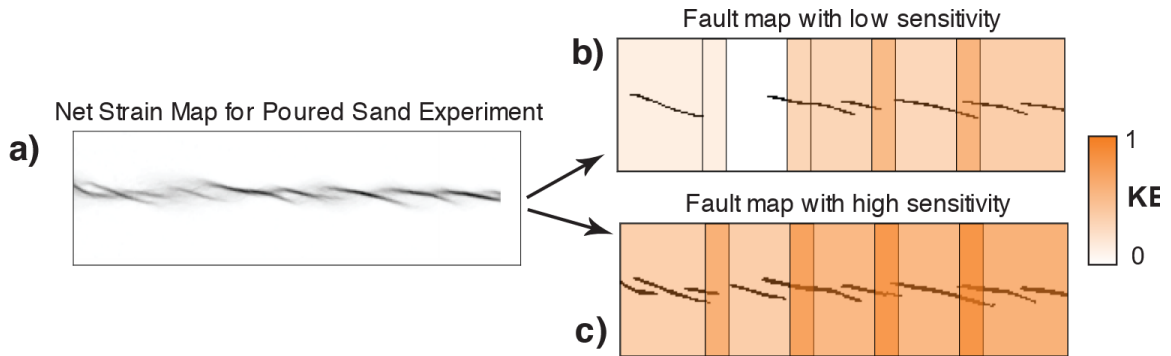
Figure 3.3: a) Incremental Net strain map from poured sand experiment and **(b-c)** fault maps with different fault detection sensitivity. **b)** Fault maps detected with low sensitivity (5x5 px neighborhood size) exhibit thinner and fewer faults than fault maps detected with c) larger neighborhood size (9x9 px) even though they both derive from the same net strain map. Saturation of each window indicates the kinematic efficiency that varies with the sensitivity of the fault map detection.

After applying the adaptive threshold technique to detect areas of high net incremental strain, we apply one last set of filters to the fault maps to reduce noise. High strain regions with fewer than 8 connected pixels are removed from the active fault maps.

Some experiments also have noisy net strain maps in the low strain regions far from the zone of applied basal shear and we filter these regions to avoid false detection of faults following Chaipornkaew et al. (2022). The result of this process is a set of binary fault map windows from each stage of each experiment that show the active fault configuration.

The CNN training also requires each fault map to have a label in order to learn the relationships between fault geometry and off-fault deformation. We use kinematic efficiency (KE), the ratio of incremental strike-slip accommodated along the fault in the direction parallel to loading to the total incremental displacement (e.g., Hatem et al., 2017), as the label to train and test the CNN on experimental fault maps. The off-fault deformation is the portion of the total applied loading that is not expressed as slip (KE = 1 – off fault deformation) (Hatem et al., 2017).

In all materials, the first early array of echelon segments have relatively low kinematic efficiency of 50-60% (high off-fault deformation) that evolve into continuous mature strike-slip fault segments with higher kinematic efficiency of 80-90% (low off-fault deformation) (e.g., Hatem et al., 2017; Visage et al., 2023). The successfully trained CNN will predict the kinematic efficiency of strike-slip faults given just an active fault map.

For each stage of the experiments and for each 64x128 px window, we calculate the average and standard deviation of the kinematic efficiency (KE), the portion of shear strain accommodated along faults. We calculate the average KE and standard deviation of KE values found by integrating the shear strain within the active fault maps regions along the 64 transects perpendicular to the applied loading within each window. Consequently,

each fault map window used to train the CNN has both an average kinematic efficiency and the associated standard deviation of KE across the window. Following Chaipornkaew et al. (2022), we use both the KE labels and the standard deviation in the custom loss function that optimizes and assesses the CNN performance.

At the start of the experiments, shear strain is distributed until the first localized echelon faults emerge on the surface of the clay. Consequently, the early active fault maps are largely null except for occasional noise. To prevent that early noise from being considered a valid active fault map, we limit the fault maps used for CNN training to those with average kinematic efficiency greater than 0.02. The first fault maps with KE > 0.02 capture the very earliest stage of strike-slip faulting that have only a few small echelon faults. After filtering out early fault maps prior to the initiation of active faulting, we have 9050 input fault maps for wet kaolin, 8364 for poured sand, and 6742 for sedimented sand.

3.3.1.1.1.1 Data split for the CNN

Developing the CNN requires three independent data groups, one used for training, another for evaluating the given model and assisting in tuning hyperparameters, and a third dataset for testing the final CNN model once training is completed. We separate the fault maps generated from each set of experimental conditions (e.g., basal friction, thickness, loading rate, and basal shear material) into three groups: training, validation, and testing. We randomly distribute the largest amount of fault map windows to training, followed by validation, and then testing.

When we split the dataset, we allocate the whole time series of each fault map window to its chosen group so that the evaluation and testing are not conditioned by training and testing on the same fault maps. With this approach, all datasets are statistically equivalent as they contain samples from all experiment configurations.

We use the following split ratio for each suite of experiments: ~70% for training the network, ~20% for validating the performance of the CNN on fault maps unseen during training, and ~10% for assessing the CNN's performance on unseen fault maps during training and validation once the learning stage is completed (Figure 3.4).
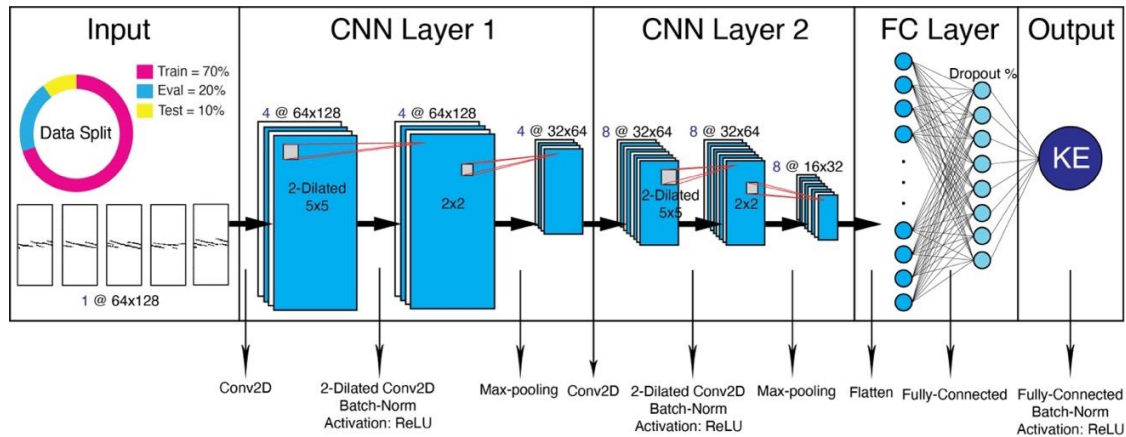
Figure 3.4: Convolutional neural network used to individually train each dataset modified from Chaipornkaew et al. (2022). The data split for all datasets is as follow: ~70% training, ~20% evaluation, and ~10% testing. Modified from Chaipornkaew et al. 2022.

3.3.1.1.1.1.1 CNN Architecture and Optimization

We utilize the CNN architecture developed by Chaipornkaew et al. (2022) and sketched in figure 4 but with stricter loss function (described below) and we use a grid

search of optimal hyperparameters for each dataset. We follow Chaipornkaew et al. (2022) and use ImageDataGenerator class of TensorFlow's Keras to process mini batches and apply subtle geometric transformations such as flipping, zooming, and shifting to introduce variations in the active fault maps (Shorten & Khoshgoftaar, 2019). Flipping of the fault maps means that regardless of whether the experiments produced right-lateral or left-lateral faults, the maps used for training will have both right and left-lateral fault maps. Shifting of the fault maps ensures that the faults are not always centered within the map. We do not tilt the faults maps because different fault orientation would yield different off-fault deformation. Instead, we ensure that the shear loading is parallel to top and bottom of the fault maps.

All CNNs employ the Adam optimizer with a modified stochastic gradient descent with a prescribed learning rate and follow a convolutional neural architecture inspired by LeNet-5 and AlexNet networks (Krizhevsky et al., 2012; Lecun et al., 1998) that use stacked convolutional layers with kernel sizes and dilation parameters. This allows the detection of small-scale features such as stepovers between echelon faults and large-scale patterns like fault connectedness.

To improve learning and performance, we follow Chaipornkaew et al. (2022) and incorporate batch normalization and use the rectified linear activation function (ReLU) followed by max-pooling (Kulathunga et al., 2021). Max-pooling highlights the most significant features in each fault map, reduces the number of parameters, and increases computing efficiency before the layer is flattened into a vector for the fully connected layers.

To prevent overfitting of the data, we apply a dropout rate before the final layer (Figure 3.4; Srivastava et al., 2014). Furthermore, we perform a hyperparameter grid search for each dataset to enhance learning and accuracy of the neural network. Hyperparameters of batch-size, learning rate, momentum, and dropout rate were iteratively tuned until reaching the optimal combination that resulted in the minimum loss in the validation dataset (see table S3 in appendix).

The CNN models are trained using a custom loss function that assesses if a prediction is correct. The custom loss function calculates the squared difference of the predicted and the truth value (KE label) based on a normalized mean square error (MSE) (Srivastava et al., 2014). The CNN model has a correct prediction of the KE label if the difference between the predicted KE and the label KE is within one standard deviation, SD, of the label. This loss function is stricter than that used by Chaipornkaew et al. (2022) that allowed correct predictions within two standard deviations of the label KE.

To prevent overfitting of the label, all models have an imposed early stopping that stops the network from training when the model no longer improves its accuracy on the validation data set. We select the final model based on the lowest loss in the validation dataset and the highest accuracy in the batch for both the training and validation datasets and use this model to predict kinematic efficiency on fault maps from the testing set. Additionally, we conduct multiple iterations with the consistent final hyperparameters combinations while altering the initial randomizations to ensure the reproducibility of each CNN model's performance.

3.4 Results

The different experimental materials, wet kaolin, poured sand, sedimented, and sieved sand, produce different early active fault patterns and similar mature strike-slip fault patterns. The earliest faults in the wet kaolin and poured sand are echelon fault segments that form at an angle relative to the basal fault and have strike-slip (Hatem et al., 2017; Lefevre et al., 2020; Visage et al., 2023). These echelon faults have been called 'R'-type Riedel shears in some studies (e.g., Lefevre et al., 2020). In the wet kaolin and poured sand experiments, the echelon segments are each planar and generally link up via new segments that develop at the center of the echelon segments and above the basal shear (Figure 3.2a and c). Eventually, the faults link and form a continuous active fault that may contain some irregularities that are relicts of the early echelon segments.

The early echelon faults within the denser sand packs of the sedimented and sieved sand produce significant dilation at the onset of faulting and generate early immature faults that have patterns distinct from faults within wet kaolin and poured sand. The first faults to form have a sigmoidal shape where the distal ends trend parallel to the applied loading direction and accommodate reverse slip (Figure 3.2b).

The central portions of the faults trend around 30° from the applied shear and accommodate predominantly strike-slip. These early faults link via new segments that parallel the loading and form across the centers of the early echelon faults. Once linked, the distal reverse slip portions of the early faults are abandoned. As with the other materials, the continuous active fault may have irregularities that reflect the early fault configuration.

3.4.1 Testing CNNs on Experimental Fault Maps

We train and evaluate the CNN individually on wet kaolin, poured sand, and sedimented sand and then test each trained CNN on its corresponding testing set to assess the predictive power of the CNN. Our results demonstrate that all CNNs have KE prediction accuracy >90% on datasets unseen during training and validation (Figures 3.5-3.7). The CNN model trained on wet kaolin achieves the greatest prediction accuracy (93%; Figure 3.5c), while CNN models trained on poured sand and sedimented sand predict with 92% (Figure 3.6c) and 91% (Figure 3.7c) KE accuracy, respectively.

In this study, the wet kaolin trained CNN achieves a 3% higher prediction accuracy than the CNN previously trained by Chaipornkaew et al. (2022) that used the same experimental dataset and a less strict custom loss function than applied here.

The improvement in accuracy can be attributed to several factors. First, each window was widened to better capture the stepover of echelon faults (Figure 3.2). This adjustment likely improved the CNN's ability to learn and understand fault patterns. Second, the elimination of fault maps with early noise (KE<0.02) cleaned the dataset, which improved the model accuracy. Lastly, the optimization of hyperparameters using the refined dataset further improved the CNN's performance despite using a stricter loss function.
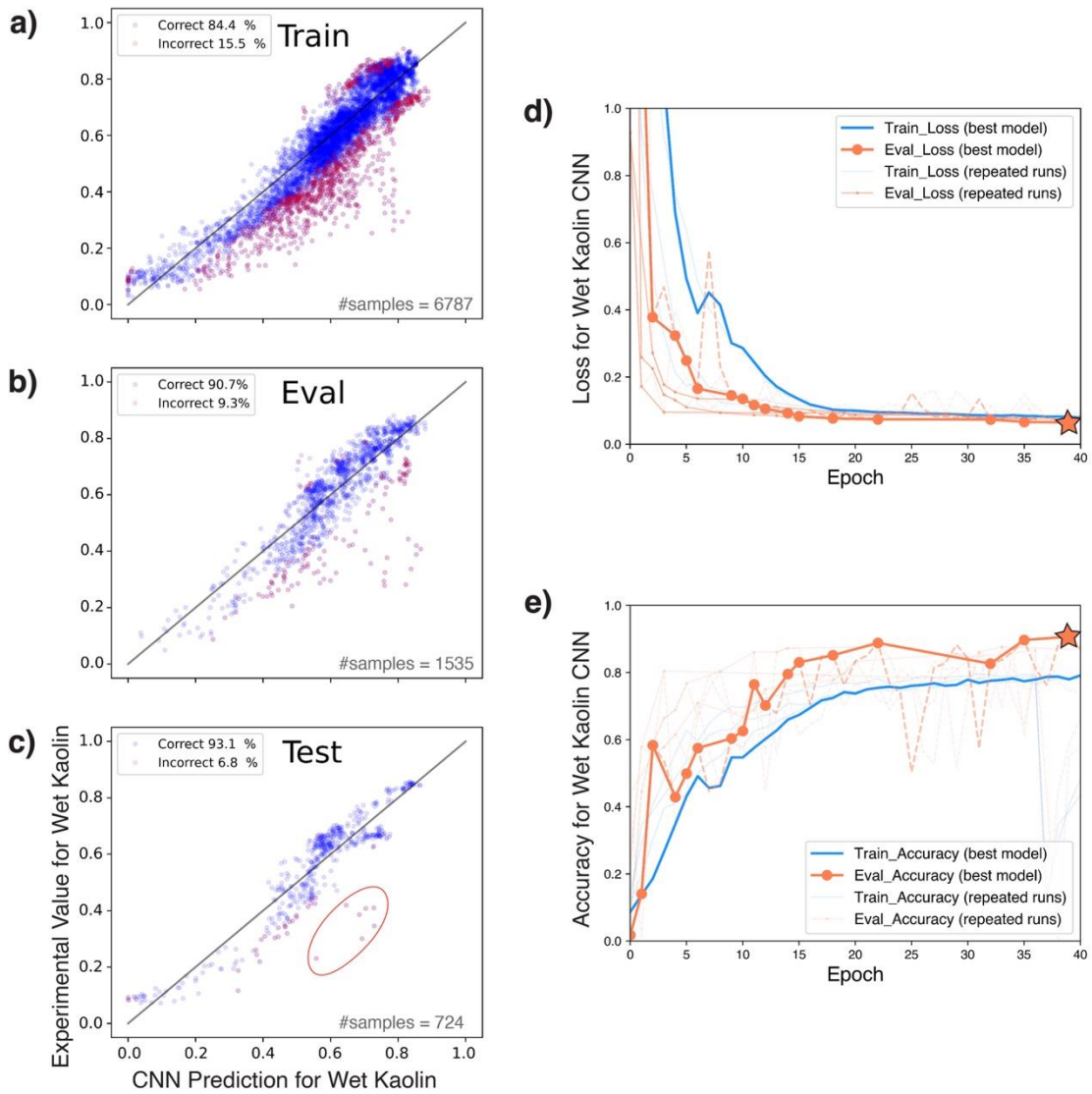
Figure 3.5: Results from **a)** training, **b)** evaluating, and **c)** testing the CNN on the wet kaolin dataset. The trained CNN can predict KE of unseen fault maps during testing with 93% accuracy. Red circle on c) indicates fault maps for which the CNN has overpredicted the KE label (underpredicted off-fault deformation). **d)** Loss and **e)** accuracy of the model as we train over 40 epochs and evaluate the performance at the end of each epoch. We impose an early stopping to prevent the model from overfitting (denoted by the star). Solid lines represent the best-performing model and translucent lines are repeated runs using the final hyperparameter combination.
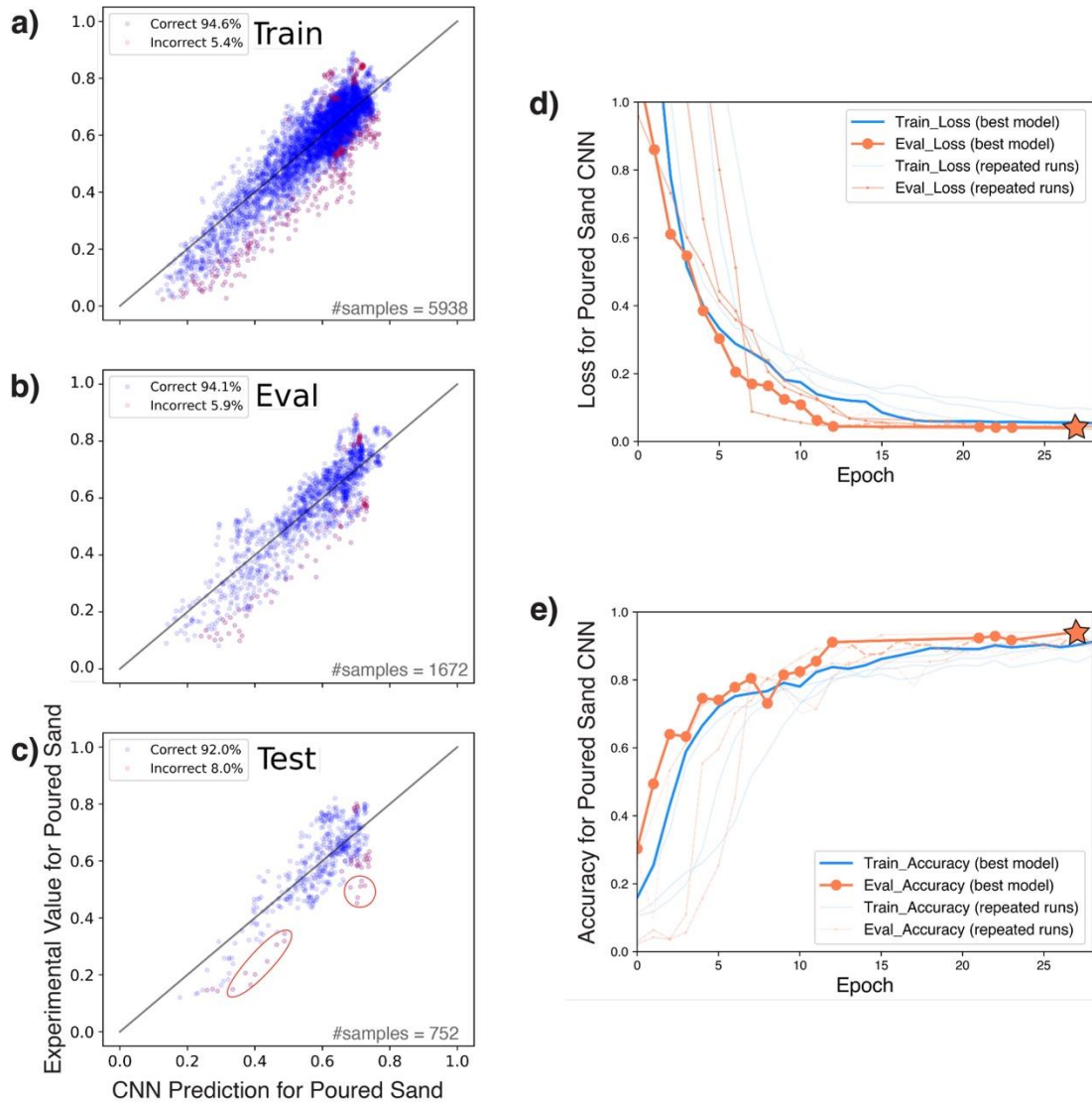
Figure 3.6: Results from **a)** training, **b)** evaluating, and **c)** testing the CNN on the poured sand dataset. Trained CNN can predict KE of unseen fault maps with 92% accuracy. Red circle on c) indicates fault maps for which the CNN has overpredicted the KE label (underpredicted off-fault deformation). **d)** Loss and **e)** accuracy of the model as we train over 20 epochs and evaluate the performance at the end of each epoch. Solid lines represent the best-performing model and translucent lines are repeated runs using the final hyperparameter combination.
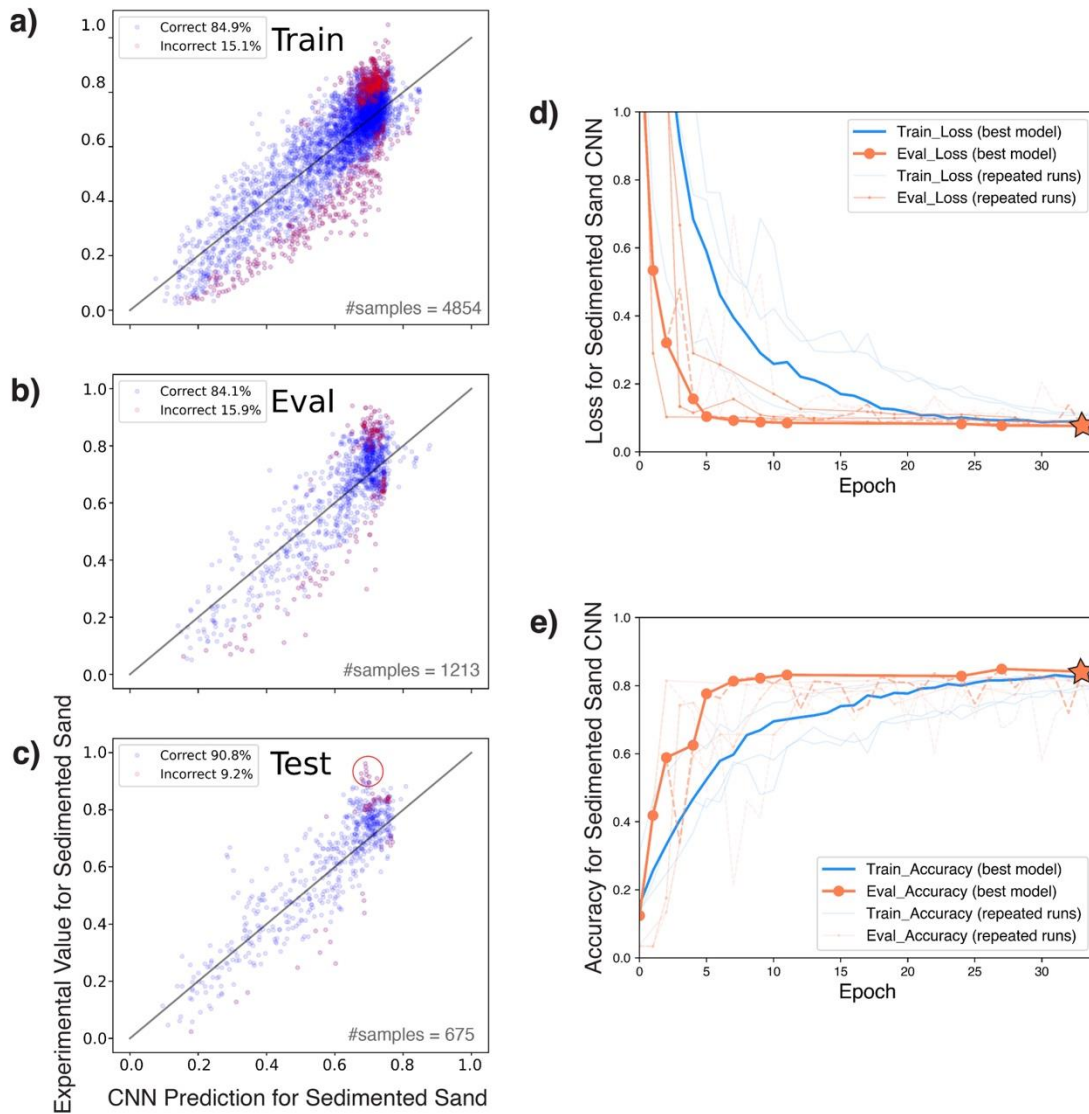
Figure 3.7: Results from **a)** training, **b)** evaluating, and **c)** testing the CNN on the sedimented sand dataset. Trained CNN can predict KE of unseen fault maps with 91% accuracy. Red circle on c) indicates the fault maps for which the CNN has underpredicted the KE label (overpredicted off-fault deformation). **d)** Loss and **e)** accuracy of the model as we train over 30 epochs and evaluate the performance at the end of each epoch. Solid lines represent the best-performing model and translucent lines are repeated runs using the final hyperparameter combination.

The wet kaolin, poured, and sedimented sand trained CNNs have different

patterns for mispredictions. Most of the wet kaolin and poured sand fault maps that

deviate by more than one standard deviation from the label during testing tend to

overpredict KE (see red circle on Figures 3.5c & 3.6c). These overpredictions of the

kinematic efficiency occur at early to mid-stages of fault maturity (KE < 0.6). For these

wet kaolin and poured sand faults maps, both CNNs underpredict off-fault deformation.

On the other hand, the sedimented sand trained CNN tends to underpredict the KE label

(overpredict off-fault deformation) on unseen test datasets (see red circle on Figure 3.7c).

This underprediction of sedimented sand occurs mostly for mature fault traces (KE >

0.8). All CNN models achieve a high accuracy during testing, demonstrating their

effectiveness in predicting kinematic efficiency on experimental active fault maps.

3.4.1.1 Testing Fault Threshold Sensitivity

Various approaches to delineate localized fault slip from distributed deformation

can potentially yield different fault maps (e.g., Hatem et al., 2017; Lefevre et al., 2020;

Visage et al., 2023). Having different fault maps will generate different KE labels (e.g.,

Figure 3.3), which might influence the predicting power of the CNN. Here, we assess

whether the trained convolutional neural networks can successfully predict the kinematic

efficiency of fault maps generated with different fault detection sensitivity. By testing

each previously trained CNN on fault maps generated with varying neighborhood sizes

we can evaluate the sensitivity of the predictions to different fault maps (e.g., Figure 3.3).

All three experiment trained CNN models perform reasonably well with predictions that

range from 65% for sedimented sand (Figure 3.8c) to 94% for poured sand (Figure 3.8b).
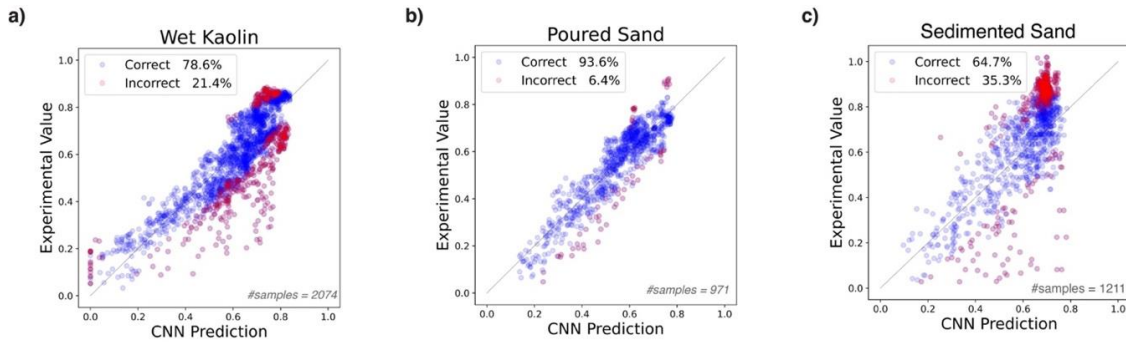
Figure 3.8: a) Results from testing the wet kaolin trained CNN on fault maps with varying levels of fault sensitivity from experiments EB_050_3 and PP_050_2, **b)** testing the poured sand trained CNN on experiments E441 and E457 and, **c)** testing the sedimented sand trained CNN on experiments E369, E338, E458, and E461. All CNNs can reasonably well predict the kinematic efficiency of fault maps defined using different detection thresholds.

The outliers from all three tests where the CNN failed to predict the KE label within one standard deviation belong to fault maps with low to high sensitivities (see Figure S1 in appendix). This result suggests that the predictive performance of the CNN does not depend on the fault detection threshold. All CNNs, especially the poured sand trained CNN, have effectively learned to generalize and make consistent predictions across fault maps that were defined in different ways.

3.4.1.1.1 Testing the CNNs on Synthetic Fault Traces

To better understand the nature of the predictions made by each trained CNN, we test each CNN on synthetic fault maps representing various stages of strike-slip fault maturity. The synthetic fault maps were inspired from field mapping studies of strike-slip faults conducted or compiled by Guo et al. (2023) and Manighetti et al. (2021), as well as the time-series of active fault maps for experiments with wet kaolin, poured sand, and sedimented sand (Figure 3.2a-c). We apply each trained CNN to fault map windows of

three synthetic faults representing very immature, immature, and mature fault traces according to definitions and quantitative metrics of fault maturity by Guo et al. (2023) and Manighetti et al (2021) (Figure 3.9a-c). The approximate KE values that we would expect for the very immature fault trace ranges from 40-55%, 55-65% for the immature fault trace, and KE values > 75% for the mature fault trace. These expected values are approximated from the analysis of fault maps from all stages of fault maturity for experiments in all three datasets and their corresponding KE labels per stage and crustal studies that provide estimates of off-fault deformations (Antoine et al., 2021, 2022; Milliner et al., 2016; Scott et al., 2019; Shelef & Oskin, 2010).
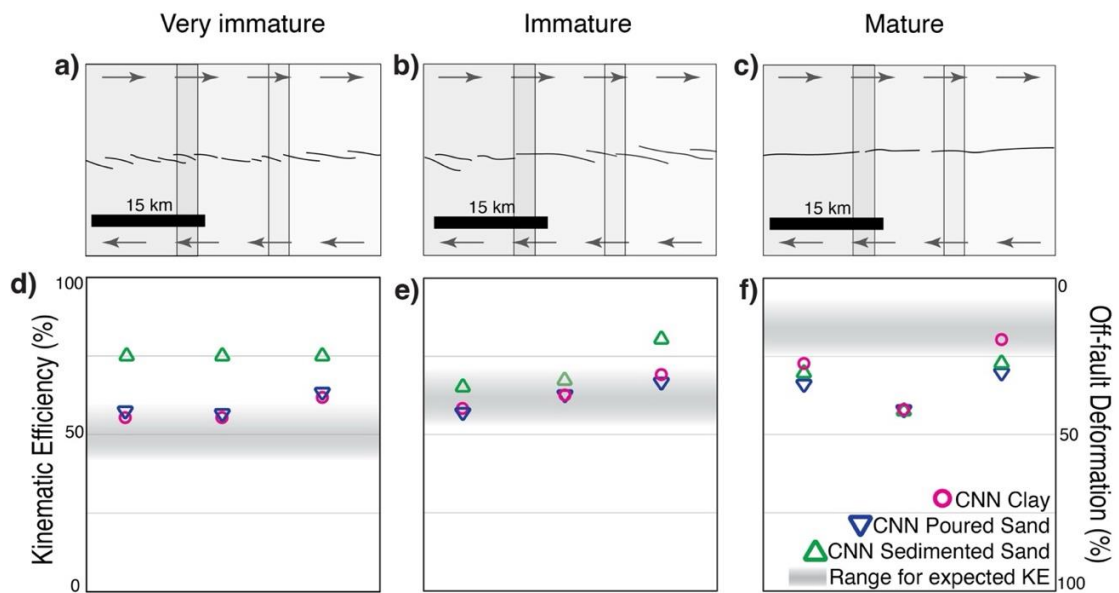
Figure 3.9: Synthetic strike-slip fault maps for **a)** very immature, **b)** immature, and **c)** mature fault traces (see Figure 3.2a-c). **(d-e)** The clay and poured sand trained CNNs have consistent predictions that overlap our expectations for very immature and immature fault traces while the sedimented sand predicts lower off-fault deformation. **f)** In contrast, the wet kaolin trained CNN predicts the highest kinematic efficiency values for the mature fault trace while the sedimented and poured sand predict greater off-fault deformation.

The predictions of the CNN on the synthetic fault maps reveal that both the CNNs trained on wet kaolin and poured sand have overlapping predictions of kinematic efficiency for the very immature and immature fault traces. The predictions of these CNN are also within the range of our estimated KE for the less mature fault traces (Figure 3.9d-e). On the other hand, the CNN trained on sedimented sand consistently predicts higher kinematic efficiency values (corresponding to lower off-fault deformation) for the very immature and immature fault traces. The sedimented sand CNN predictions exceed the expected KE values for the very immature fault trace (Figure 3.9d) but are within the expected KE range for the immature fault trace (Figure 3.9e).

The CNNs prediction of kinematic efficiency for the mature fault trace depend on whether the active fault trace is continuous across the window or has a gap (Figure 3.9c). The CNN trained on wet kaolin predicts the highest KE values that are also within our estimated range for windows that capture a continuous segment of the fault trace. In contrast, the poured and sedimented sand trained CNNs have lower KE predictions for these windows that overlap each other (Figure 3.9f). All three CNNs provide similar KE estimates for the middle active fault map window that captures a gap along the otherwise mature fault trace. We expect lower off-fault deformation (higher KE values) on the smoother sections of a fault trace than on segmented portions and this is confirmed by all three CNNs (Figure 3.9f).

The CNN trained on sedimented sand predicts higher KE values for the segmented very immature fault traces (Figure 3.9d) than for the smooth sections of the mature fault trace (Figure 3.9f) that are inconsistent with both our expectations and the predictions of the CNN trained on other materials. The inconsistency of the sedimented

sand trained CNN predictions for these synthetic faults of varying maturity/roughness indicates that this CNN may be a less reliable predictor for off-fault deformation around strike-slip faults than the CNN trained on other materials.

Overall, the CNN trained on sedimented sand consistently underestimates the off-fault deformation of very segmented and immature fault traces (Figure 3.9d), while both the wet kaolin and poured sand trained CNNs predict reasonable estimates of the off-fault deformation on very immature and immature faults.

3.4.1.1.1.1 Testing CNNs on Experimental Fault Maps from Different Rheology

Can CNN trained on one material that simulates upper crustal deformation successfully predict the partitioning of strain on faults produced in another material? We assess the performance of all three CNNs by testing each CNN on all experimental fault maps of other materials to determine their ability to predict the kinematic efficiency of fault maps generated from experiments conducted with different materials that are all viable analogs for upper crustal deformation (Figure 3.10). In addition to testing each trained CNN with other materials, we test each CNN on the G12 sieved sand experiments run at the GFZ Potsdam laboratory. When assessing the performance of the predictions, we determined that unsuccessful predictions have <50% accuracy, acceptable predictions have up to 70% accuracy, good predictions have up to 90% accuracy, and exceptional predictions have >90% accuracy when predicting the kinematic efficiency label on unseen dataset.
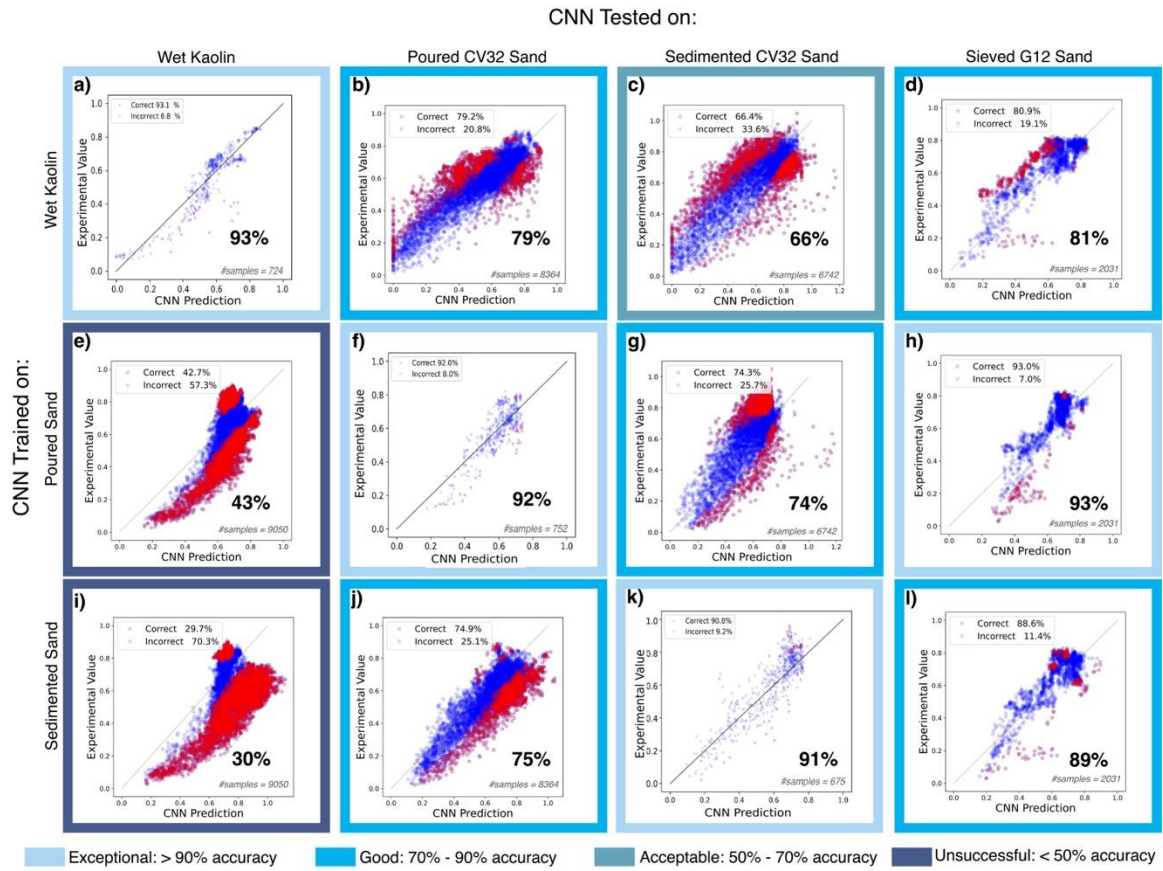
Figure 3.10: The color of thick boxes around each plot indicates the goodness of the trained CNN on predicting kinematic efficiency. CNN trained on wet kaolin has overall the best performance at predicting kinematic efficiency of fault maps with different rheology properties. The CNN trained on CV32 sand performs well at predicting KE of fault maps in G12 sand experiments. However, both CNNs trained on poured and sedimented sand obtain low results when predicting KE of fault maps in wet kaolin.

The CNN trained on wet kaolin provides acceptable or good predictions off-fault deformation at all stages of fault evolution in poured, sedimented, and sieved sand. The wet kaolin trained CNN makes good predictions when tested on poured and sieved G12 sand fault maps (Figure 3.10b and d) and makes acceptable predictions for sedimented CV32 sand fault maps (Figure 3.10c). Most mispredictions outside of one standard deviation belong to fault maps where the CNN has underpredicted KE values (overpredicted off-fault deformation) of poured, sedimented/sieved sand fault maps.

These underpredicted KE values are from fault maps from all stages of fault maturity in poured and sedimented CV32 sand but only from mid-late stages (KE = 0.5-0.8) in sieved G12 sand.

The poured sand trained CNN predicts well the strain partitioning of other sand (Figure 3.10g and h) but cannot predict off-fault deformation of active fault maps in wet kaolin (Figure 3.10e). The model has unsuccessful predictions when tested on clay fault maps at all levels of maturity, but the poured sand trained CNN can predict the kinematic efficiency of fault maps in sedimented sand with moderately good accuracy (Figure 3.10g) and on sieved G12 sand fault maps with exceptional accuracy (Figure 3.10h). Most of the failed predictions when tested on the sedimented sand dataset are mature fault maps (KE > 0.7) where the CNN model underpredicts the KE label (Figure 3.10g). In contrast, the few outliers when testing the poured sand trained CNN on sieved G12 sand active fault maps arise from immature fault traces (KE < 0.3).

Like the poured sand trained CNN, the sedimented sand trained CNN predicts well strain partitioning of other sand (Figure 3.10j and l) but cannot predict off-fault deformation of active fault maps in wet kaolin (Figure 3.10i). The sedimented sand trained CNN incorrectly predicts off-fault deformation of active fault maps from all stages of strike-slip fault maturity in wet kaolin (Figure 3.10i) and has a lower predicting accuracy than the poured sand trained CNN (Figure 3.10e). The sedimented sand trained CNN makes good predictions of KE for active fault maps with different maturity in poured sand with overpredictions of KE at all levels of fault maturity (Figure 3.10j). Similarly, the sedimented sand trained CNN makes good predictions of strain partitioning

on the sieved G12 sand fault maps with a few overpredictions of KE at all levels of fault maturity (Figure 3.10l).

3.4.1.1.1.1.1 Combining all Experimental Datasets for Training and Testing

Can the CNN trained on an extensive experimental dataset that draws from three different crustal analog materials provide a wider range of fault evolution patterns to better capture crustal deformation? We assess this question by creating a new dataset that encompasses experiments on wet kaolin, sedimented sand, and poured sand. We combine all three datasets to train and test the convolutional neural network to assess its predicting power and subsequently apply this more comprehensively trained CNN on crustal fault maps (see discussion). We maintain the same data split used for individually trained CNN models (see tables S1 and S2 in appendix) and utilize the same CNN architecture used for all models (Figure 3.4). Because the combined experimental dataset has greater complexity than each individual type of analog material, the CNN trained on the combined data learns differently. For this reason, we perform a new extensive grid search of hyperparameters instead of using the previous hyperparameter combinations determined for each dataset (see table S3 in appendix).

We test the CNN model on an unseen test dataset that encompasses a combination of active fault maps in wet kaolin, sedimented sand, and poured sand from all stages of fault maturity. The CNN trained on the combined dataset has 87% accuracy of KE predictions when tested on an unseen dataset (Figure 3.11c). Outliers that fall outside one standard deviation during testing arise from fault maps of all maturity levels where the

CNN overpredicts KE (underpredicts off-fault deformation). These results suggest that the CNN trained on experiments from all three materials representing a range of rheology has learned to estimate KE from fault geometry that developed in different materials. The CNN trained on all three materials provides good predictions of off-fault deformation from all levels of fault maturity.
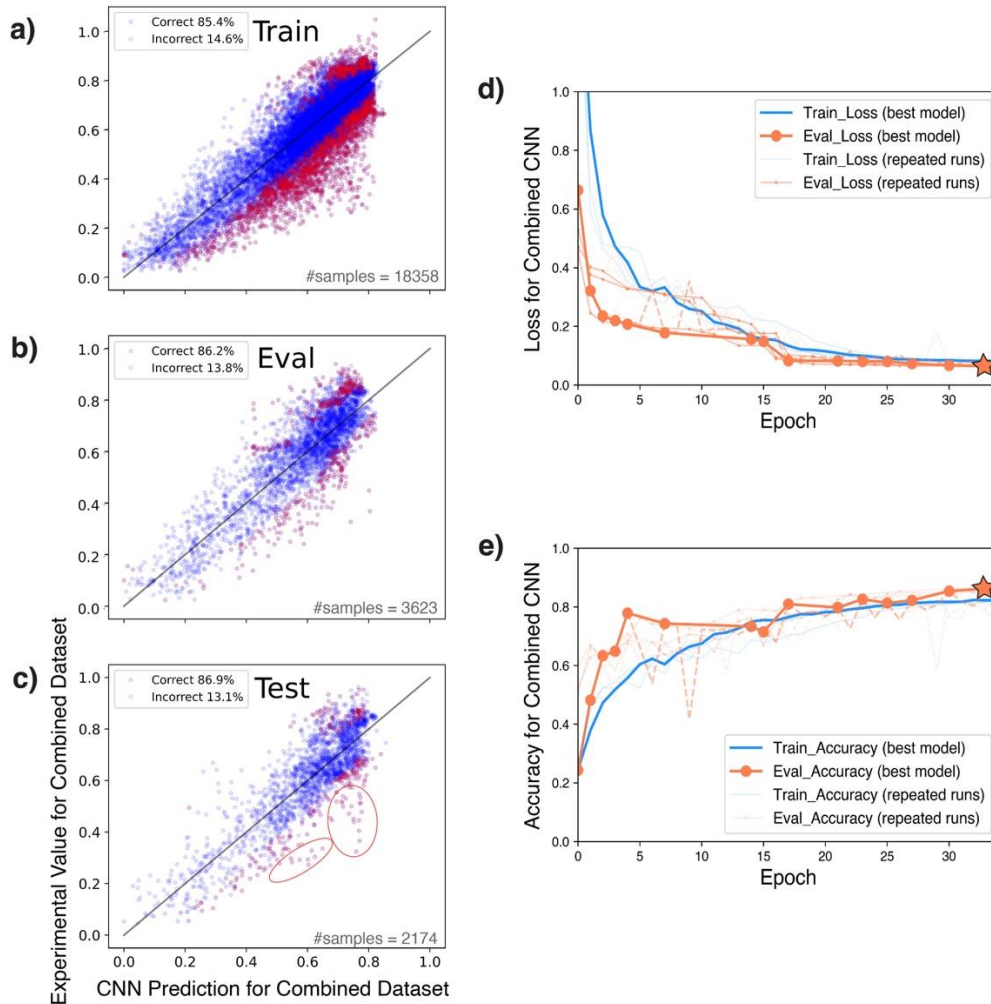
Figure 3.11: Results from a) training, b) evaluating, and c) testing the CNN on the wet kaolin + sedimented sand + poured sand datasets. Trained CNN can predict KE of unseen fault maps with 87% accuracy. d) Loss and e) accuracy of the model as we train over 30 epochs and evaluate the performance at the end of each epoch. Red circle indicates outliers where the CNN has overpredicted KE (underpredicted off-fault deformation) of immature to mid-mature fault maps (KE < 0.65). Solid lines represent the best-performing model and translucent lines are repeated runs using the final hyperparameter combination.

3.5. Discussion

3.5.1 Testing on Crustal Fault Maps

Because scaled physical experiments use materials that are designed to simulate upper crustal deformation, the CNN trained on experimental strike-slip faults can inform strain partitioning along and off of fault of crustal strike-slip fault traces (Chaipornkaew et al., 2022). To assess the potential of using experimental trained CNNs on crustal fault maps, we compare the off-fault deformation estimates from four geologic studies to the predictions made by the experiment trained CNNs that use the active fault maps of the geologic studies. These geologic studies estimate off-fault deformation accumulated across different time spans: coseismic deformation associated with the 2019 Ridgecrest mainshock (Figure 12a; Antoine et al., 2021; Milliner et al., 2021), coseismic deformation associated with the 2016 M7 Kumamoto earthquake along the Futagawa fault (Figure 12b; Scott et al., 2019), bending of Mesozoic faults and dikes adjacent to the northern Calico fault in the Eastern California Shear Zone (Figure 12c; Shelef & Oskin, 2010), and Holocene deformation of drainages on the northwest side of the San Andreas fault at Mecca Hills (Figure 12d; Gray et al., 2018).

The Futagawa fault, the northern Calico fault, and the San Andreas fault at Mecca Hills, were also analyzed by Chaipornkaew et al. (2022). We keep the three fault maps in our analysis because they provide varying levels of fault maturity and off-fault deformation estimates accumulated across different periods. Also, we tune the workflow for creating the fault maps, widen the fault maps windows to three times the echelon length to better capture stepovers, and exclude fault maps with early occasional noise (KE < 0.02) (see method section). Because we have improved the training dataset and

hyperparameter search from that of Chaipornkaew et al. (2022) leading to a higher model

accuracy for the wet kaolin trained CNN in our study (Figure 3.5), we can expect

differences in the predictions of KE for the same crustal fault maps. Furthermore,

because we widen the fault map windows for training, we have also widened the crustal

fault map windows. Consequently, our study has fewer but wider fault map windows than

that of Chaipornkaew et al. (2022) that capture stepovers for all crustal maps.
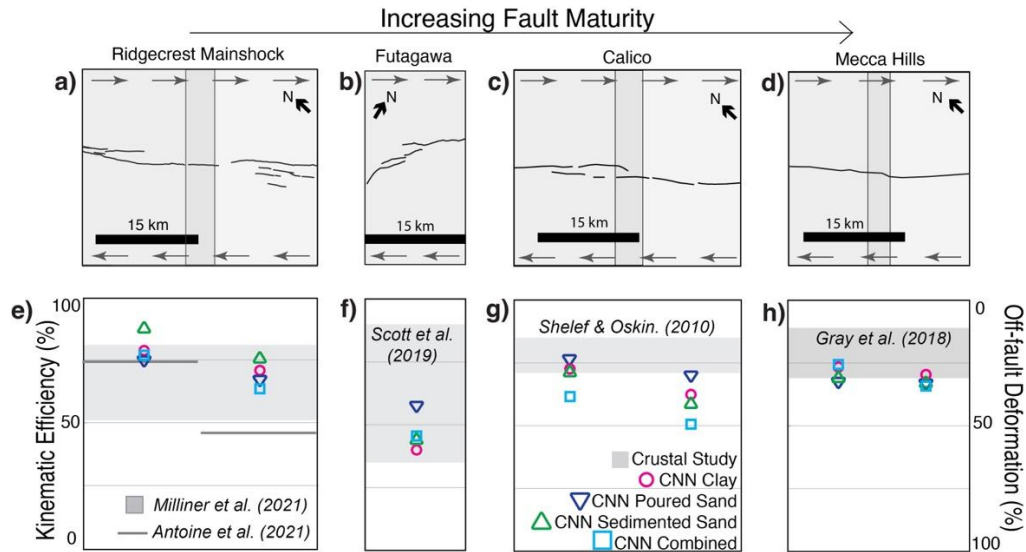
Figure 12. CNN models applied to crustal fault trace maps and the kinematic efficiency ranges from each geologic study (gray rectangles) and the CNN predictions for each model denoted by symbols and colors in legend. **a)** Coseismic displacement associated with the 2019 Mw. 7.1 Ridgecrest Mainshock (Antoine et al., 2021; Milliner et al., 2021), **b)** coseismic deformation associated with the 2016 M7 Kumamoto earthquake along the Futagawa fault (Scott et al., 2019), **c)** bending of Mesozoic faults and dikes near Calico fault (Shelef & Oskin, 2010), and **d)** deflected drainages at Mecca Hills (Gray et al., 2018). **e)** The KE predictions made by all CNNs are almost all within the off-fault deformation range provided by Milliner et al. (2021) but only the predictions made for the left window overlap with the estimated value by Antoine et al. (2021). **f)** All CNNs predict KE values for the Futagawa fault within the range of crustal study; the poured sand trained CNN predicts the highest KE. **g)** For the Calico fault only the wet kaolin, poured, and sedimented sand overlap the crustal study's estimate for off-fault deformation for the left window. The combined trained CNN predicts greater off-fault deformation than other CNN for both windows. **h)** A few of the CNNs overlap with Gray et al. (2018) value for off-fault deformation along San Andreas fault (between grey and blue lines). All active fault maps from each of the geologic studies are oriented so that the regional maximum shear direction, determined from GNSS data, is consistent with the shear loading of fault maps in our experiments (i.e., along the top and bottom of each 64x128 pixel fault map window).

This study includes the Ridgecrest Mainshock for which we have two estimates for off-fault deformation (Figure 3.12a). Milliner et al. (2021) considered off-fault deformation along the whole rupture (grey box on Figure 3.12e) while Antoine et al. (2021) calculated estimates for different portions of the mainshock rupture (grey line on Figure 3.12e). The predictions made by the CNNs trained on experimental data with wet kaolin, poured sand, sedimented sand, and the combination of those materials are almost all within the ranges of off-fault deformation provided by Milliner et al. (2021) for the 2019 Ridgecrest Mainshock (Figure 3.12e). All CNNs predict higher KE (lower off-fault deformation) for the left (northwest) window of the Ridgecrest crustal map, which has less mature fault trace than the right (southeast) window. All CNNs, except for the sedimented sand trained CNN, provide KE values that overlap with the off-fault deformation value provided by Antoine et al. (2021) for the left window of the fault trace but they all predict higher KE values (lower off-fault deformation) for the right portion of the fault trace (Figure 3.12e). Furthermore, the sedimented sand trained CNN predicts the highest KE values of all the models for both fault maps windows of the segmented Ridgecrest mainshock rupture; this CNN makes similar predictions for the very immature synthetic fault trace on Figure 3.9d.

Most of the CNN KE predictions for the Futagawa crustal fault in the Kumamoto earthquake are within the range of Scott et al (2019) for off-fault deformation (Figure 3.12b). The sedimented sand and combined CNN predict KE values that overlap each other. Similarly, the wet kaolin trained CNN predicts high off-fault deformation while the poured sand trained CNN predicts lower off-fault deformation for the same section of the fault trace (Figure 3.12f).

Some of the experiment trained CNNs predict KE within Shelef and Oskin's (2010) range for off-fault deformation along the Calico fault (Figure 3.12g). The wet kaolin, poured sand, and sediment sand trained CNNs provide KE predictions that are within the off-fault deformation range for Calico's left window that captures two segmented semi parallel faults whereas, the combined trained CNN predicts a higher off-fault deformation for the same fault portion (Figure 3.12b and g). For the right window (southeast) that captures a less geometrically complex section (one active fault strand) of the fault trace, all CNNs predict higher off-fault deformation values than for the left (northwest) window. The off-fault deformation values predicted by each CNN fall outside range estimate by Shelef and Oskin. (2010) with the highest KE prediction by the poured sand trained CNN and the lowest KE (greatest off-fault deformation) prediction by the combined trained CNN (Figure 3.12g). Out of all models, the combined trained CNN consistently predicts higher off-fault deformation for all crustal fault map windows along the Calico fault, especially for the right-most (southeast) window.

Most experiment trained CNN predictions for the mature San Andreas fault at Mecca Hills overlap the kinematic efficiency estimates for the Calico fault (Figure 3.12d). The off-fault deformation estimates from Gray et al. (2018) are based on measurements of 3.5 ± 1.5 mm/yr of drainage deflection within 800 m on the northeast side of the fault. If the southwest side of the San Andreas fault, which was not analyzed, also experiences 3.5 ± 1.5 mm/yr of off-fault deformation, then the total off-fault deformation along this fault may be 11-29% of the 35-40 mm/yr slip rate on this fault. Because the San Andreas dips northeast, the off-fault deformation may be greater on the northeast side of the fault so we will consider 29% as a maximum with likely values

90

between 10 and 25%. All the experiment trained CNN models agree with each other and predict off-fault deformation similar to the crustal estimates (Figure 3.12h).

The CNN model trained on the combined experimental dataset predicts kinematic efficiency that overlaps the other experimental trained CNNs for most of the four crustal fault maps (Figure 3.12e-h). This consistency probably suggests that the wet kaolin and poured sand trained CNN models contributed greatly to the combined training.

Overall, the CNN models predict the highest off-fault deformation for the segmented Futagawa fault and similar but lower off-fault deformation for the Ridgecrest mainshock, Calico fault, and San Andreas fault at Mecca Hills (Figure 3.12a-d). Most of the CNN predictions of off-fault deformation match geologic estimates, demonstrating that experimental trained CNN can be used to provide estimates of off-fault deformation and the degree of shallow slip-deficit on strike-slip faults using the fault trace and known regional loading orientation.

We can compare the crustal fault KE predictions made by the wet kaolin trained CNN in our study to the predictions estimated by the CNN of Chaipornkaew et al. (2022). For the three crustal fault maps that were used in both studies, the differences between KE predictions of the two CNN vary across all fault map windows. The Futagawa fault KE predictions by the wet kaolin trained CNN are lower in our study than KE predictions of Chaipornkaew et al. (2022). On the other hand, our KE predictions for the Calico fault are higher and within the range of predictions for each of the narrower fault map windows used by Chaipornkaew et al. (2022). For the San Andreas fault at Mecca Hills our KE predictions are similar to those of Chaipornkaew et al. (2022). The slight differences in KE predictions between our wet kaolin trained CNN and

Chaipornkaew et al. (2022) could be due to various reasons. We train our CNN model on a smaller but improved dataset and with a different combination of hyperparameters. Furthermore, we test on fewer but wider fault map windows that better capture stepovers than Chaipornkaew et al. (2022), which could explain the variations in KE predictions.

3.5.1.1 CNN Application to the San Jacinto Fault Trace

We can apply the experimental trained CNN model to predict off-fault deformation along strike-slip faults for which we do not yet have geologic information about strain partitioning. To demonstrate this application, we use the trace of the San Jacinto fault taken from the USGS Quaternary Fault and Fold database (USGS, accessed 2022). The active trace of the San Jacinto fault has some regions that are continuous and mature while other regions are complex with fault branches and segmented (Figure 3.13). Figure 3.13 shows the fault map windows that we use for predicting kinematic efficiency using the CNN trained on the combination of wet kaolin and dry sand fault maps, which represents the widest range of rheologic conditions.
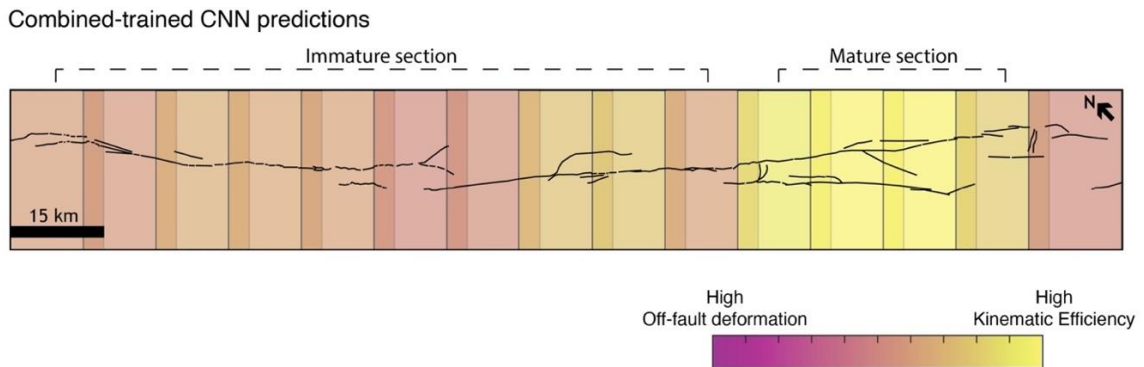
Figure 3.13: Active fault trace of the San Jacinto fault overlain on the windows used as inputs to the CNN model trained with the combination of the clay and sand fault maps. The color of each fault map window indicates the predicted off-fault deformation (pink) of that portion of the San Jacinto fault. The northwest windows that capture the immature section of the fault trace have higher degree of strain partitioned as off-fault deformation than the southeast windows that show a higher relative maturity.

The CNN model predicts a higher degree of strain partitioned as off-fault deformation (~40-50%) for segmented and corrugated fault portions (see northwest windows on Figure 3.13) that represent immature fault geometries. On the other hand, the windows where the CNN predicts higher kinematic efficiency (~80%) are smoother portions of the fault with less undulation but with branching segments (see southeast windows on Figure 3.13). The CNN trained on the combined dataset predicts patterns of off-fault deformation that are consistent with our expectations; corrugated and segmented fault trace indicate less mature fault segments with greater off-fault deformation. The lowest off-fault deformation and highest kinematic efficiency occur where two fault segments overlap so that the map window contains two parallel faults. Such geometry is not considered mature but may accommodate a significant portion of strike-slip along the two active faults. However, the experiments of this study generally only hosted a single active fault trace. Consequently, the CNN trained in this study would not reliably estimate off-fault deformation in regions with parallel active strands.

3.5.1.1.1 Limitations of the CNN

Both wet kaolin and dry sand are well suited for examining the evolution of fault structures over many earthquake cycles. Faults within the materials of experiments studied here creep and do not exhibit stick-slip behavior often realized along crustal

faults. Off-fault deformation from dynamic rupture processes occurring during earthquake events would not be captured in the experiments that simulate quasi-static deformation. For example, the experiments of this study do not capture aspects of distributed near surface deformation that may arise from the co-seismic ground shaking. The lack of these dynamic effects may cause the experiment trained CNNs to underpredict the co-seismic shallow slip deficit along crustal faults.

Co-seismic off-fault deformation estimates (e.g., Antoine et al., 2021; Milliner et al., 2021; Scott et al, 2019; Gray et al., 2018; Shelef & Oskin, 2010) do not include the distributed deformation that accumulates during the interseismic period. One might therefore expect geologic estimates of off-fault deformation to exceed co-seismic estimates for the same fault. These two factors combined, the underprediction of ground shaking effects and inclusion of at least some long-term off-fault deformation, may allow the CNN estimates to match coseismic estimates of off-fault deformation (Figure 3.12a and b). By extension, we would then expect the experiment trained CNN to underpredict off-fault deformation for the geologic estimates that include many earthquake cycles (Figure 3.12c and d) because the CNN lack ground shaking effects. One reason we might not see this for the findings of the Calico fault is that the deflected Mesozoic structures mapped by Shelef and Oskin. (2010) are within bedrock materials so that these off-fault deformation estimates do not include the shallow slip deficit that occurs in the upper few kilometers.

3.6 Conclusion

Although the geologic record does not often provide reliable estimates of off-fault deformation, we can use experimentally produced active strike-slip fault trace maps

developed within different analog materials to train Convolutional Neural Networks to predict off-fault deformation from active strike-slip fault traces. Because laboratory experiments use analog materials that are carefully scaled to reproduce crustal processes, the CNNs trained on experimental fault maps can be used to predict crustal off-fault deformation and provide estimates of the degree of shallow slip deficit along strike-slip faults, such as Figure 3.13 for the San Jacinto fault.

We show that all experiment trained CNN models (wet kaolin, poured sand, and sedimented sand) have exceptional accuracy when tested on an unseen dataset of a similar analog material (Figures 3.5c, 3.6c, and 3.7c). The CNN trained on the combined data set has good accuracy of predicting off-fault deformation on unseen fault maps from all the experiments (Figure 3.11c). The CNN trained on one material produces variable accuracy when tested on other materials (Figure 3.10). The wet kaolin trained CNN has the best overall performance with acceptable accuracy of off-fault deformation predictions on all materials (Figure 3.12b-d).

The wet kaolin and poured sand trained CNNs perform the best when predicting the off-fault deformation of synthetic and crustal faults representing different fault maturity whereas the sedimented sand trained CNNs has low prediction reliability on both synthetic and crustal faults. The off-fault deformation predictions of the combined CNN model follow the predictions of individually trained CNNs on crustal fault maps, suggesting that this CNN recognizes characteristics of fault geometry expressed by different materials that represent a range of deformation mechanisms within the upper crust. This study shows the potential for deep learning trained on experimentally

95

produced faults to estimate the strain partitioning of crustal faults which can help us

estimate the degree of shallow slip deficit along faults of differing maturity.

APPENDIX

SUPPLEMENT FOR CHAPTER 3

Experiment Name	Basal Configuration	Velocity (mm/min)	Window Width (cm)	Overlap (%)	# Windows	Neighborhood Size	Data Split
PP_025_1	Plate	0.25	11	20	5	5	Train
PP_025_2	Plate	0.25	11	20	5	5	Train/Eval/Test
PP_050_1	Plate	0.50	11	20	5	5	Train
PP_050_2	Plate	0.50	11	20	5	5	Train/Eval/Test
PP_100_1	Plate	1.0	11	20	5	5	Train
PP_100_2	Plate	1.0	11	20	5	5	Train/Eval/Test
PP_150_1	Plate	1.50	11	20	5	5	Train/Eval/Test
EB_025_1	Elastic Band	0.25	11	20	5	5	Train
EB_025_2	Elastic Band	0.25	11	20	5	5	Train
EB_025_3	Elastic Band	0.25	11	20	5	5	Train/Eval/Test
EB_050_1	Elastic Band	0.50	11	20	5	5	Train
EB_050_2	Elastic Band	0.50	11	20	5	5	Train
EB_050_3	Elastic Band	0.50	11	20	5	5	Train/Eval/Test
EB_150_1	Elastic Band	1.50	11	20	5	5	Train
EB_150_2	Elastic Band	1.50	11	20	5	5	Train
EB_150_3	Elastic Band	1.50	11	20	5	5	Train/Eval/Test

Table S1. Strike-slip fault experiments with wet kaolin used for training, evaluation, and testing. Table indicates each experiment configuration with loading conditions (mm/min), window width (cm), the amount of window overlap, the number of fault map windows obtained per experiment, and the fault sensitivity used (neighborhood size). Since each experiment configuration is repeated, we split the data into training, evaluation, and testing. To fully allocate the first experiment configuration to training and the repeated experiments divided into training, evaluation, and testing.

Experiment Name	Deposition Technique	Sand pack Thickness (cm)	Basal Material	Window Width (cm)	Overlap (%)	# Windows	Neighborhood Size	Data Split
E280	Sedimented	4	PVC	25	43	7	7	Train
E287	Sedimented	2.5	PVC	12.5	20	10	9	Train
E319	Sedimented	4	PVC	25	42	6	7	Train/Eval/Test
E320	Sedimented	4	PVC	25	50	4	5	Train/Eval/Test
E321	Sedimented	4	PVC	25	37	6	7	Train/Eval/Test
E322	Sedimented	4	PVC	25	31	6	7	Train/Eval/Test
E324	Sedimented	4	PVC	25	37	6	7	Train
E328	Sedimented	3.5	PVC	20.8	20	6	7	Train/Eval/Test
E329	Sedimented	3.5	PVC	20.8	20	6	7	Train
E331	Sedimented	3	PVC	16.7	20	8	7	Train/Eval/Test
E332	Sedimented	2.5	PVC	12.5	20	10	7	Train/Eval/Test
E345	Sedimented	5	PVC	33.3	48	5	7	Train/Eval/Test
E346	Sedimented	3.3	PVC	19.1	20	6	7	Train
E347	Sedimented	5	PVC	33.3	45	5	5	Train/Eval/Test
E353	Sedimented	3	PVC	16.7	20	8	7	Train/Eval/Test
E355	Sedimented	6	PVC	41.6	48	4	5	Train/Eval/Test
E458	Sedimented	5	PVC	33.3	45	6	7	Train/Eval/Test
E459	Sedimented	5	PVC	33.3	46	6	5	Train
E461	Sedimented	4	PVC	25	50	4	7	Train/Eval/Test
E463	Sedimented	6	PVC	41.6	50	5	5	Train/Eval/Test
E464	Sedimented	7	PVC	49.9	49	3	5	Train
E499	Sedimented	6	PVC	41.6	50	5	5	Train
E338	Sedimented	4	Alkor-foil	28.4	45	6	9	Train/Eval/Test
E339	Sedimented	3.5	Alkor-foil	23.9	40	7	7	Train/Eval/Test
E340	Sedimented	3	Alkor-foil	19.5	34	8	7	Train
E342	Sedimented	2.5	Alkor-foil	15.0	31	9	7	Train
E363	Sedimented	5	Sandpaper	44	26	3	5	Train/Eval/Test
E364	Sedimented	2	Sandpaper	8.3	20	16	9	Train
E365	Sedimented	3	Sandpaper	25	45	7	7	Train/Eval/Test
E366	Sedimented	2.5	Sandpaper	20.3	45	9	9	Train
E368	Sedimented	4	Sandpaper	34.5	48	5	7	Train/Eval/Test
E369	Sedimented	3.5	Sandpaper	29.8	46	6	9	Train
E350	Poured	4	PVC	14.7	20	8	7	Train/Eval/Test
E351	Poured	5	PVC	19.0	35	8	7	Train
E352	Poured	3.5	PVC	12.6	20	10	7	Train
E439	Poured	4	PVC	14.7	20	11	7	Train/Eval/Test
E440	Poured	4	PVC	14.7	20	12	7	Train
E441	Poured	4	PVC	14.7	20	11	7	Train/Eval/Test
E442	Poured	4	PVC	14.7	20	11	7	Train/Eval/Test
E444	Poured	4	PVC	14.7	20	11	7	Train/Eval/Test
E451	Poured	6	PVC	23.3	39	8	7	Train
E452	Poured	6	PVC	23.3	38	8	7	Train/Eval/Test
E455	Poured	7	PVC	27.6	40	7	5	Train

E456	Poured	7	PVC	27.6	43	7	5	Train/Eval/Test
E457	Poured	5	PVC	19.0	20	8	7	Train/Eval/Test
E481	Poured	6	PVC	23.3	46	7	5	Train/Eval/Test
E482	Poured	6	PVC	23.3	50	7	5	Train/Eval/Test
E483	Poured	6	PVC	23.3	39	8	7	Train/Eval/Test
E484	Poured	6	PVC	23.3	39	8	7	Train/Eval/Test
E494	Poured	6	PVC	23.3	20	7	7	Train/Eval/Test

Table S2. Strike-Slip fault experiments with dry sand CV32 indicating deposition technique, thickness of sandpack (cm), basal frictional material, window width (cm), the amount of window overlap (%), the number of fault map windows obtained per experiment, and the fault sensitivity (neighborhood size) used per experiment. The data split consists of allocating all windows of the first experiment configuration to training and the repeated experiment configurations divided into training, evaluation, and testing. Allowing training to get most of the windows, followed by evaluation, and the least windows for testing.

Hyperparameters	Search Ranges	Selected Values for Wet Kaolin	Selected Values for Poured Sand	Selected Values for Sedimented Sand	Selected Values for Combined
#Kernels in the first CNN layer	4 - 8	4	4	4	4
Learning Rate	1e-5 – 1e-2	5e-3	9e-3	3e-3	1e-3
Batch Size	8 - 512	256	256	128	128
Momentum	0.60 - 0.99	0.60	0.65	0.95	0.65
Dropout Rate	10% - 30%	30	30	25	15

Table S3. Hyperparameters grid search for all three distinct CNN networks and for the combined CNN network trained in all three datasets.
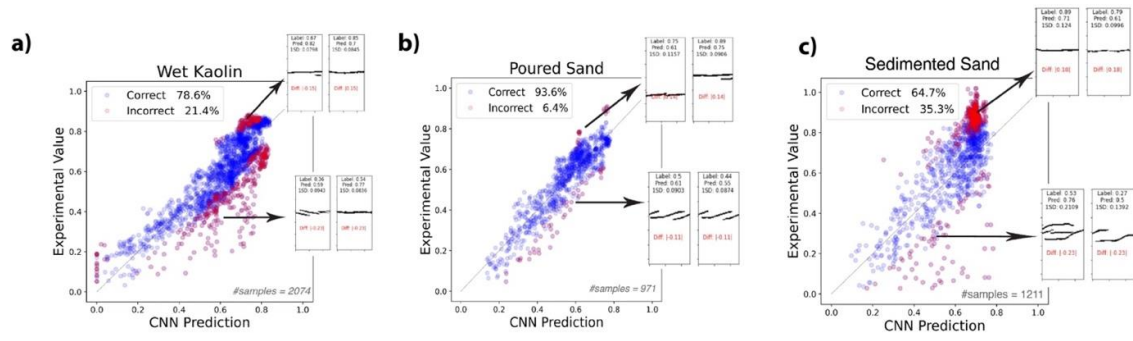
Figure S1. Outliers outside one standard deviation of the label when testing a) the wet kaolin trained CNN, b) poured sand, and c) sedimented sand on fault maps with different maturity. Outliers belong to fault maps with different sensitivities from all stages of fault evolution.

BIBLIOGRAPHY

Adam, J., Urai, J.L., Wieneke, B., Pfeiffer, K., Kukowski, N., Lohrmann, J., Hoth, S., Van Der Zee, W., Schmatz, J. (2005). Shear localization and strain distribution during tectonic faulting: new insights from granular-flow experiments and high-resolution optical image correlation techniques. Journal of Structural Geology, 27, 283-301. https://doi.org/10.1016/j.jsg.2004.08.008

Antoine, S., Klinger, Y., Wang, K., & Bürgmann, R. (2023). Diffuse deformation explains the magnitude-dependent coseismic shallow slip deficit [Preprint]. In Review. https://doi.org/10.21203/rs.3.rs-2536085/v1

Antoine, S. L., Klinger, Y., Delorme, A., & Gold, R. D. (2022). Off-Fault Deformation in Regions of Complex Fault Geometries: The 2013, M_w 7.7, Baluchistan Rupture (Pakistan). Journal of Geophysical Research: Solid Earth, 127(11), e2022JB024480. https://doi.org/10.1029/2022JB024480

Antoine, S. L., Klinger, Y., Delorme, A., Wang, K., Bürgmann, R., & Gold, R. D. (2021). Diffuse Deformation and Surface Faulting Distribution from Submetric Image Correlation along the 2019 Ridgecrest, California, Ruptures. Bulletin of the Seismological Society of America, 111(5), 2275–2302. https://doi.org/10.1785/0120210036

Bemis, S. P., Micklethwaite, S., Turner, D., James, M. R., Akciz, S., Thiele, S. T., & Bangash, H. A. (2014). Ground-based and UAV-Based photogrammetry: A multi-scale, high-resolution mapping tool for structural geology and paleoseismology. *Journal of Structural Geology*, *69*, 163–178. https://doi.org/10.1016/j.jsg.2014.10.007

Bonanno, E., Bonini, L., Basili, R., Toscani, G., & Seno, S. (2017). How do horizontal, frictional discontinuities affect reverse fault-propagation folding? *Journal of Structural Geology*, *102*, 147–167. https://doi.org/10.1016/j.jsg.2017.08.001

Bonini, L., Basili, R., Toscani, G., Burrato, P., Seno, S., & Valensise, G. (2016). The effects of pre-existing discontinuities on the surface expression of normal faults: Insights from wet-clay analog modeling. Tectonophysics, 684, 157–175. https://doi.org/10.1016/j.tecto.2015.12.015

Bonini, L., Fracassi, U., Bertone, N., Maesano, F. E., Valensise, G., & Basili, R. (2023). How do inherited dip-slip faults affect the development of new extensional faults? Insights from wet clay analog models. Journal of Structural Geology, 169, 104836. https://doi.org/10.1016/j.jsg.2023.104836

Chaipornkaew, L., Elston, H., Cooke, M., Mukerji, T., & Graham, S. A. (2022). Predicting Off-Fault Deformation From Experimental Strike-Slip Fault Images Using Convolutional Neural Networks. Geophysical Research Letters, 49(2). https://doi.org/10.1029/2021GL096854

Chester, F.M., Chester, J.S., (1998). Ultracataclasite structure and friction processes of the Punchbowl fault, San Andreas system, California. Tectonophysics, 295, 199-221. https://doi.org/10.1016/S0040-1951(98)00121-8

Cooke, M. L., Schottenfeld, M. T., & Buchanan, S. W. (2013). Evolution of fault efficiency at restraining bends within wet kaolin analog experiments. Journal of Structural Geology, 51, 180–192. https://doi.org/10.1016/j.jsg.2013.01.010

Cooke, M. L., & Van Der Elst, N. J. (2012). Rheologic testing of wet kaolin reveals frictional and bi-viscous behavior typical of crustal materials: RHEOLOGIC TESTING OF WET KAOLIN. Geophysical Research Letters, 39(1), n/a-n/a. https://doi.org/10.1029/2011GL050186

Cubas, N., Maillot, B., & Barnes, C. (2010). Statistical analysis of an experimental compressional sand wedge. Journal of Structural Geology, 32(6), 818–831. https://doi.org/10.1016/j.jsg.2010.05.010

Davis, G. H., Bump, A. P., García, P. E., & Ahlgren, S. G. (2000). Conjugate Riedel deformation band shear zones. *Journal of Structural Geology*, 22(2), 169–190. https://doi.org/10.1016/S0191-8141(99)00140-6

Dotare, T., Yamada, Y., Adam, J., Hori, T., & Sakaguchi, H. (2016). Initiation of a thrust fault revealed by analog experiments. Tectonophysics, 684, 148–156. https://doi.org/10.1016/j.tecto.2015.12.023

Eisenstadt, G., & Sims, D. (2005). Evaluating sand and clay models: Do rheological differences matter? Journal of Structural Geology, 27(8), 1399–1412. https://doi.org/10.1016/j.jsg.2005.04.010

Elston, H., Cooke, M., & Hatem, A. (2022). Non-steady-state slip rates emerge along evolving restraining bends under constant loading. Geology, 50(5), 532–536. https://doi.org/10.1130/G49745.1

Fang, Z., & Dunham, E. M. (2013). Additional shear resistance from fault roughness and stress levels on geometrically complex faults. Journal of Geophysical Research: Solid Earth, 118(7), 3642–3654. https://doi.org/10.1002/jgrb.50262

Guo, H., Lay, T., & Brodsky, E. E. (2023). Seismological Indicators of Geologically Inferred Fault Maturity. Journal of Geophysical Research: Solid Earth, 128(10), e2023JB027096. https://doi.org/10.1029/2023JB027096

Hatem, A. E., Cooke, M. L., & Madden, E. H. (2015). Evolving efficiency of restraining bends within wet kaolin analog experiments. Journal of Geophysical Research: Solid Earth, 120(3), 1975–1992. https://doi.org/10.1002/2014JB011735

Hatem, A. E., Cooke, M. L., & Toeneboehn, K. (2017). Strain localization and evolving kinematic efficiency of initiating strike-slip faults within wet kaolin experiments. Journal of Structural Geology, 101, 96–108. https://doi.org/10.1016/j.jsg.2017.06.011

Henza, A. A., Withjack, M. O., & Schlische, R. W. (2010). Normal-fault development during two phases of non-coaxial extension: An experimental study. Journal of Structural Geology, 32(11), 1656–1667. https://doi.org/10.1016/j.jsg.2009.07.007

Hubbert, M. K. (1937). Theory of scale models as applied to the study of geologic structures. Geological Society of America Bulletin, 48(10), 1459–1520. https://doi.org/10.1130/GSAB-48-1459

Kaneko, Y., & Fialko, Y. (2011). Shallow slip deficit due to large strike-slip earthquakes in dynamic rupture simulations with elasto-plastic off-fault response: Modelling shallow slip deficit. Geophysical Journal International, 186(3), 1389–1403. https://doi.org/10.1111/j.1365-246X.2011.05117.x

Klinkmüller, M., Schreurs, G., Rosenau, M., & Kemnitz, H. (2016). Properties of granular analogue model materials: A community wide survey. Tectonophysics, 684, 23–38. https://doi.org/10.1016/j.tecto.2016.01.017

Krizhevsky, A., Sutskever, I., & Hinton, G. E. (2017). ImageNet classification with deep convolutional neural networks. Communications of the ACM, 60(6), 84–90. https://doi.org/10.1145/3065386

Kulathunga, N., Ranasinghe, N. R., Vrinceanu, D., Kinsman, Z., Huang, L., & Wang, Y. (2021). Effects of Nonlinearity and Network Architecture on the Performance of Supervised Neural Networks. Algorithms, 14(2), 51. https://doi.org/10.3390/a14020051

Lecun, Y., Bottou, L., Bengio, Y., & Haffner, P. (1998). Gradient-based learning applied to document recognition. Proceedings of the IEEE, 86(11), 2278–2324. https://doi.org/10.1109/5.726791

Lefevre, M., Souloumiac, P., Cubas, N., & Klinger, Y. (2020). Experimental evidence for crustal control over seismic fault segmentation. Geology, 48(8), 844–848. https://doi.org/10.1130/G47115.1

Li, C., Li, T., Shan, X., & Zhang, G. (2023). Extremely Large Off-Fault Deformation during the 2021 Mw 7.4 Maduo, Tibetan Plateau, Earthquake. Seismological Research Letters, 94(1), 39–51. https://doi.org/10.1785/0220220139

Lohrmann, J., Kukowski, N., Adam, J., & Oncken, O. (2003). The impact of analogue material properties on the geometry, kinematics, and dynamics of convergent sand wedges. Journal of Structural Geology, 25(10), 1691–1711. https://doi.org/10.1016/S0191-8141(03)00005-1

Maillot, B. (2013). A sedimentation device to produce uniform sand packs. Tectonophysics, 593, 85–94. https://doi.org/10.1016/j.tecto.2013.02.028

Manighetti, I., Mercier, A., & De Barros, L. (2021). Fault Trace Corrugation and Segmentation as a Measure of Fault Structural Maturity. Geophysical Research Letters, 48(20), e2021GL095372. https://doi.org/10.1029/2021GL095372

Milliner, C., Donnellan, A., Aati, S., Avouac, J., Zinke, R., Dolan, J. F., Wang, K., & Bürgmann, R. (2021). Bookshelf Kinematics and the Effect of Dilatation on Fault Zone Inelastic Deformation: Examples From Optical Image Correlation Measurements of the 2019 Ridgecrest Earthquake Sequence. Journal of Geophysical Research: Solid Earth, 126(3). https://doi.org/10.1029/2020JB020551

Milliner, C. W. D., Dolan, J. F., Hollingsworth, J., Leprince, S., & Ayoub, F. (2016). Comparison of coseismic near-field and off-fault surface deformation patterns of the 1992 M_w 7.3 Landers and 1999 M_w 7.1 Hector Mine earthquakes: Implications for controls on the distribution of surface strain. Geophysical Research Letters, 43(19). https://doi.org/10.1002/2016GL069841

Nevitt, J. M., Brooks, B. A., Hardebeck, J. L., & Aagaard, B. T. (2023). 2019 M7.1 Ridgecrest earthquake slip distribution controlled by fault geometry inherited from Independence dike swarm. *Nature Communications*, *14*(1), 1546. https://doi.org/10.1038/s41467-023-36840-2

Nevitt, J. M., Brooks, B. A., Catchings, R. D., Goldman, M. R., Ericksen, T. L., & Glennie, C. L. (2020). Mechanics of near-field deformation during co- and post-seismic shallow fault slip. Scientific Reports, 10(1), 5031. https://doi.org/10.1038/s41598-020-61400-9

Okubo, K., Bhat, H. S., Rougier, E., Marty, S., Schubnel, A., Lei, Z., Knight, E. E., & Klinger, Y. (2019). Dynamics, Radiation, and Overall Energy Budget of Earthquake Rupture With Coseismic Off-Fault Damage. *Journal of Geophysical Research: Solid Earth*, *124*(11), 11771–11801. https://doi.org/10.1029/2019JB017304

Panien, M., Schreurs, G., & Pfiffner, A. (2006). Mechanical behaviour of granular materials used in analogue modelling: Insights from grain characterisation, ring-shear tests and analogue experiments. Journal of Structural Geology, 28(9), 1710–1724. https://doi.org/10.1016/j.jsg.2006.05.004

Pollitz, F. F., Murray, J. R., Svarc, J. L., Wicks, C., Roeloffs, E., Minson, S. E., Scharer, K., Kendrick, K., Hudnut, K. W., Nevitt, J., Brooks, B. A., & Mencin, D. (2020). Kinematics of Fault Slip Associated with the 4–6 July 2019 Ridgecrest, California, Earthquake Sequence. Bulletin of the Seismological Society of America, 110(4), 1688–1700. https://doi.org/10.1785/0120200018

Reber, J. E., Cooke, M. L., & Dooley, T. P. (2020). What model material to use? A Review on rock analogs for structural geology and tectonics. Earth-Science Reviews, 202, 103107. https://doi.org/10.1016/j.earscirev.2020.103107

Rudolf, M., Rosenau, M., & Oncken, O. (2023). Time-dependent frictional properties of granular materials used in analogue modelling: Implications for mimicking fault healing during reactivation and inversion. Solid Earth, 14(3), 311–331. https://doi.org/10.5194/se-14-311-2023

Saucier, F., Humphreys, E., & Weldon, R. (1992). Stress near geometrically complex strike-slip faults: Application to the San Andreas fault at Cajon Pass, southern California. Journal of Geophysical Research, 97(B4), 5081–5094. https://doi.org/10.1029/91jb02644

Scott, C., Champenois, J., Klinger, Y., Nissen, E., Maruyama, T., Chiba, T., & Arrowsmith, R. (2019). The 2016 M7 Kumamoto, Japan, Earthquake Slip Field Derived From a Joint Inversion of Differential Lidar Topography, Optical Correlation, and InSAR Surface Displacements. Geophysical Research Letters, 46(12), 6341–6351. https://doi.org/10.1029/2019GL082202

Shelef, E., & Oskin, M. (2010). Deformation processes adjacent to active faults: Examples from eastern California. Journal of Geophysical Research, 115(B5), B05308. https://doi.org/10.1029/2009JB006289

Shorten, C., & Khoshgoftaar, T. M. (2019). A survey on Image Data Augmentation for Deep Learning. Journal of Big Data, 6(1), 60. https://doi.org/10.1186/s40537-019-0197-0

Srivastava, N., Hinton, G., Krizhevsky, A., Sutskever, I., & Salakhutdinov, R. (2014). Dropout: A Simple Way to Prevent Neural Networks from Overfitting.

Thielicke, W., & Stamhuis, E. J. (2014). PIVlab – Towards User-friendly, Affordable and Accurate Digital Particle Image Velocimetry in MATLAB. Journal of Open Research Software, 2. https://doi.org/10.5334/jors.bl

Toeneboehn, K., Cooke, M. L., Bemis, S. P., Fendick, A. M., & Benowitz, J. (2018). Stereovision Combined With Particle Tracking Velocimetry Reveals Advection and Uplift Within a Restraining Bend Simulating the Denali Fault. Frontiers in Earth Science, 6, 152. https://doi.org/10.3389/feart.2018.00152

Visage, S., Souloumiac, P., Cubas, N., Maillot, B., Antoine, S., Delorme, A., & Klinger, Y. (2023). Evolution of the off-fault deformation of strike-slip faults in a sand-box experiment. Tectonophysics, 847, 229704. https://doi.org/10.1016/j.tecto.2023.229704

Withjack, M. O., Schlische, R. W., & Henza, A. A. (2007). Scaled Experimental Models of Extension: Dry Sand vs. Wet Clay.